QUEST RJ

ISSN 1605-8607
Bi-Annual

QUAID-E-AWAM UNIVERSITY RESEARCH JOURNAL OF ENGINEERING SCIENCE & TECHNOLOGY

QUAID-E-AWAM UNIVERSITY RESEARCH JOURNAL of Engineering, Science & Technology

MISSION STATEMENT OF QUEST

"To provide quality and state-of-the art education (coursework, practical training and research) in prescribed branches of Engineering and Science to the enrolled students in order to make them better professionals and better human being; so that they become capable of contributing amicably towards national development".

Volume 14 No: 1 JAN. - JUNE 2015

BI-ANNUAL **ISSN 1605-8607**

QUAID-E-AWAM UNIVERSITY RESEARCH JOURNAL OF ENGINEERING, SCIENCE & TECHNOLOGY

EDITORIAL BOARD

ANNUAL SUBSCRIPTION..... RS. 200.00 (INLAND0, US$ 20.00 (FOREIGN, BY SURFACE MAIL)
SINGLE ISSUE.....RS. 100.00 (INLAND0, US$ 10.00 (FOREIGN, BY SURFACE MAIL)

The Bi-Annual Quaid-e-Awam University Research Journal of Engineering, Science & Technology, shall be supplied free of cost in exchange of Research Journal(s) from other Universities/Institutions and Research Centers.

BI-ANNUAL **ISSN 1605-8607**

ACKNOWLEDGEMENT

The members of Editorial Board, Quaid-e-Awam University Research Journal of Engineering, Science & Technology are grateful for valuable and critical suggestions on various research paper(s) sent to following Researchers/Experts for Volume 14, No. 1, January – June 2015 issue. The members also appreciate the Referees/Experts for sharing their knowledge and expertise towards improvement of standard of this research Journal.

Professor Ali Akbar Ranjbar
Director of International Affairs,
Babol University of Technology,
Iran

Dr. Ramzan Luhur
Department of Mechanical Engg
Quaid-e-Awam University of
Engineering, Science & Technology,
Pakistan

Dr. Malek Shams
École Centrale de Nantes,
France

Dr. Rafiq Ahmed Sayer
Campus Kirchberg,
Université du, Luxembourg

Dr. Muhammad Farrukh Shahab
City University London,
United Kingdom

Professor Pierluigi Siano
Department of Industrial Engg:
University of Salerno, Italy

Dr. Dur Muhammad Soomro
Dept: of Electrical Power Engineering
Faculty of Electrical and Electronic
Engineering. Universiti Tun Hussein Onn,
Malaysia (UTHM)

Prof. Zubair Memon
Department of Electrical Engineering,
Mehran University of Engineering &
Technology, Pakistan

Dr. Charbel Habchi
Department of Mechanical
Engineering (MENG),
Lebanese International University,
Lebanon

Dr. Muhammad Kashif
University of Central Punjab,
Pakistan

Dr. Malik Mubashir Hasan
Université de Versailles Saint-Quentin-
en-Yvelines (UVSQ),
France

Dr. Saad Missen
Université de la Rochelle,
France

Dr. Ali Hanzala Khan
Åbo Akademi University,
Finland

Dr. Muhammad Ahsan Latif
Department of Computer Science,
University of Agriculture, Faisalabad,
Pakistan

BI-ANNUAL **ISSN 1605-8607**

CONTENTS

VOLUME 14 **NO. 1** **JANUARY – JUNE 2015**

AN OPTIMALLY ACCURATE SPECTRAL VOLUME FORMULATION WITH SYMMETRY PRESERVATION

Fareed Hussain Mangi*, Umair Ali Khan**, Intesab Hussain Sadhayo**, Rameez Akbar Talani***, Asif Ali Memon*

ABSTRACT

High order accuracy has become a challenge in numerical simulations for engineering applications. A number of methods have been developed which provide adequate levels of accuracy in numerical simulations. Among them, the Spectral Volume (SV) method is the most effective approach that ensures local conservation and achieves high order accuracy for unstructured grids. A number of formulations for SV method have been reported and tested. However, these formulations are inconsistent and/or do not preserve the symmetry property of an elliptical operator. In this paper, we propose a new formulation, named as Symmetry Preservation in Spectral Volume (SPSV) for spectral volume method that is not only consistent and stable, but also preserves the symmetry property of an elliptical operator. We test the newly proposed formulation on diffusion equation and Burger equation using different boundary conditions and evaluate it with respect to symmetry preserving capability, accuracy, and stability. Furthermore, we also present a detailed comparison between the local SV and the SPSV formulation. Our results show that besides preserving the symmetry of an elliptical operator, the SPSV formulation is more accurate and stable.

Keywords: *spectral volume method; symmetry preserving; diffusion equation.*

1. INTRODUCTION

The Spectral Volume (SV) [1-3] and Discontinuous Galerkin (DG) [4] are two popular high-order methods for hyperbolic conservation laws capable of handling unstructured grids. The critical analysis of DG and SV methods show that they both can achieve high order accuracy on unstructured grids, but take more memory as compared to the conventional second-order method. They are also similar in efficiency. The SV method appears to have a higher resolution for discontinuities because the data limiting can be done at the sub-element level. The SV method is based on two major points: (i) flux reconstruction at the interface taking into account the physics of the problem under consideration, and (ii) reconstructing high-order polynomials within spectral volumes to achieve higher accuracy. SV method particularly differs from other methods, e.g., k-exact finite volume and its variants [7-12] with respect to data reconstruction. SV method does not consider a large number of adjacent cells to reconstruct a polynomial. Instead, it divides a simple grid cell into a number of sub-cells. The average values of these sub-cells which represent the solution unknown are the inputs to the polynomial reconstruction process. An appropriate approximation approach, e.g., Riemann solver can be used to compute the numerical flux with the formulated solutions at both sides of a given interface. In the subsequent step, the traditional finite volume method [13] can be used to update the solution unknowns to higher accuracy.

The spectral volume method comprising the above mentioned steps is known to be effective for hyperbolic conservation laws, including nonlinear systems on unstructured grids [1-3]. It can successfully solve nonlinear time-dependent hyperbolic systems of conservation laws using a number of schemes including explicit method, Runge Kutta time integration [14], Riemann method, and total variation bounded non-limiters [15]. The ability of SV method to deliver high accuracy, geometrical flexibility and conservation has been confirmed by a number of studies. The spectral volume method has also been successfully applied for the Euler's equations. In order to extend it to the Navier-Stokes equations, three different formulations have been tested by Yuzhiet al. [16] for the diffusion term: (i) naïve implementation on diffusion equation, (ii) implementation of Galerkin method [17], and (iii) inclusion of a penalty factor in the numerical flux which is similar to the methods described in [18-20]. The first formulation is found to be inconsistent in a number of numerical analysis. On the other hand, although the local SV and the penalty SV formulations are consistent and stable, there are still some drawbacks that need to be improved. For the local SV formulation, the symmetry property of an elliptic operator is not preserved. Consequently the numerical solution to a symmetric physical problem will not be symmetric. For the penalty SV formulation, the order of accuracy of the method may be the same as the order of the polynomial used for the reconstruction. For example, with quadratic reconstruction, only second order

* Department of Energy & Environment Engineering,

** Department of Computer Systems Engineering,

*** Department of Electrical Engineering

Quaid-e-Awam University of Engineering, Science & Technology, Nawabshah.
email: fareedmangi@gmail.com, umair.khan@quest.edu.pk

accuracy can be achieved for diffusion equation, while third order accuracy can be obtained for first order equation.

In this paper, a new formulation for the SV method is proposed which preserves the symmetry property of the elliptic operator. In addition, with degree of polynomial reconstruction, we can obtain order accuracy for convection-diffusion equation on uniform grid. This formulation is referred to as Symmetry Preservation in Spectral Volume (SPSV) scheme for SV method.

This paper is structured as follows. Section 2 gives a brief account of the spectral volume method. Section 3 describes the traditional local SV formulation. In section 4, we discuss our proposed SV method, referred to as Symmetry Preservation in Spectral Volume (SPSV) scheme. Section 5 provides an in-depth accuracy analysis, discussion on stability issues, and numerical evaluation of the proposed scheme for diffusion equation and Burger equation along with comparisons with the local SV formulation. Section 6 concludes the paper.

2. SPECTRAL VOLUME METHOD

We first briefly discuss the principle of the spectral volume proposed by Wang [1]. For simplicity, only one-dimensional case will be considered in this paper. Let us consider a scalar convection-diffusion equation.

$$\frac{du}{dt} + \frac{df(u(x,t))}{dx} = \frac{d}{dx}(\mu \frac{du}{dx}), \qquad in[a,b]x[0,T] \tag{1}$$

Given a partition of the domain $[a,b]$, $\{x_{i+1/2}\}_{i=0}^{N}$, the domain is then divided into N non-overlapping spectral volumes, i.e.,

$$[a,b] = \cup_{i=1}^{N} S_i, \quad S_i = [x_{i-1/2}, x_{i+1/2}] \tag{2}$$

Let $h_i = x_{i+1/2} - x_{i-1/2}$, and denote the quantity $\max_{1\le i\le N} h_i$ by h. Given a desired numerical order of accuracy k for equation (1), each spectral volume S_i is subdivided into k Control Volumes (CV) using the following partitioning with $\{x_{i+1/2}\}_{j=0}^{k}$ with $x_{i,1/2} = x_{i-1/2}$ and $x_{i,k+1/2} = x_{i+1/2}$. The j^{th} CV of S_i is then given by equation (3).

$$C_{i,j} = (x_{i,j-1/2}, x_{i,j-1/2}), \quad j = 1,\dots,k \tag{3}$$

The state variable representing the average values of cells at time t for $C_{i,j}$ is given as:

$$\bar{u}_{i,j}(t) = \frac{\int_{x_{i,j-1/2}}^{x_{i,j+1/2}} u(x,t)dx}{h_{i,j}}, \quad j = 1,\dots,k, \; i = 1,\dots,N \tag{4}$$

We employ the Lagrange interpolation polynomial to reconstruct the solution inside each SV as follows.

$$p_i(x,t) = \sum_{j=1}^{k} u_{i,j}(t) h_j(x) \tag{5}$$

with

$$h_j(x) = \prod_{s=1, s\neq j}^{k} \frac{x - x_s^c}{x_j - x_s^c} \tag{6}$$

Where $x_s^c = \frac{1}{2}(x_{i,s-1/2} + x_{i,s+1/2})$ is the center of the control volume and $u_{i,j}(t)$ is the value of the reconstruction function $p_i(x,t)$ at the center of the CV. Integration of the $p_i(x,t)$ function over each CV gives a linear equation between $u_{i,j}(t)$ and $\bar{u}_{i,j}(t)$:

$$\int_{x_{I,J-/2}}^{x_{I,J+/2}} p_i(x,t)\,dx = \Sigma \int_{x_{I,J-/2}}^{x_{I,J+/2}} u_{i,j}(t) h_j(x)\,dx = \Sigma u_{i,j}.\alpha_j = \bar{u}_{i,j}(t) \qquad j = 1,2,..k \tag{7}$$

Inversion of the above function gives the reconstruction function expressed in terms of $\bar{u}_{i,j}$. It must be noted that just like finite element method, inversion of the above system needs not to be done for each SV. It can be computed once using a mapping between a standard SV and a general SV.

This reconstruction can be solved in many ways. A unique polynomial of degree of at most $k-1$, whose cell average in each of the CVs in S_i agrees with that of $u(x)$, i.e.,

$$\bar{u}_{i,j} = \frac{\int_{x_{i,j-1/2}}^{x_{i,j+1/2}} p_i(x)dx}{h_{i,j}}, \quad j = 1,\dots,k \tag{8}$$

This polynomial $p_i(x)$ is the k^{th} order approximation we are looking for as long as the function $u(x)$ is smooth in the region covered by S_i. Ultimately, we need to compute the approximate solutions of $u(x)$ at the CV boundaries to update the state variables at the next time level. Since the mappings from the given cell averages $\bar{u}_{i,j}$ to the CV boundary values are linear, there exist coefficients c_{jl} which depend on the order of accuracy k, and on the mesh size $h_{i,j}$ in S_i, but not on the function u itself, such that,

$$u_{i,j+\frac{1}{2}} = \sum_{l=1}^{k} c_{jl}\bar{u}_{il}, j = 0,\dots,k \tag{9}$$

The detailed discussion for $c_{jl}$is given in [1]. For equal-distance partition, it is given by:

$$c_{jl} = \sum_{r=l}^{k} \frac{1}{\prod_{q=0, q\neq r}^{k} (r-q)} \sum_{m=0, m\neq r}^{k} \prod_{q=0, q\neq r,m}^{k} (j-q) \tag{10}$$

With the reconstructed state variables at the CV boundaries for all SVs, we can update each control volume as if it is independent, i.e.,

$$\frac{du_{i,j}}{dt}h_{i,j} + (f_{i,j+1/2} - f_{i,j-1/2}) = \mu[(u_x)_{i,j+1/2} - (u_x)_{i,j-1/2})], \quad (11)$$

where $f_{i,j+1/2}$ is the numerical fluxe at $x_{i,j+1/2}$. We perform time integration using 3rd order Runge-Kutta method [4] for the diffusion equation and implicit method with deffered correction is used for the Burger's eqation.

3. LOCAL SPECTRAL VOLUME FORMULATION

In the local SV formulation, equation (1) is first transformed to a first order system by introducing a new variable $q = u_x$. The resulting system is given by,

$$\begin{aligned} \frac{du}{dt} + \frac{df(u(x,t))}{dx} &= \mu\frac{dq}{dx} \\ q &= \frac{du}{dx} \end{aligned} \quad (12)$$

Integrating equation (12) over each control volume, we obtain:

$$\begin{aligned} h_{i,j}\frac{du_{i,j}}{dt} + [\hat{f}_{i,j+1/2} - \hat{f}_{i,j-1/2}] &= \mu[\hat{q}_{i,j+1/2} - \hat{q}_{i,j-1/2}] \\ q_{i,j}.h_{i,j} &= \hat{u}_{i,j+1/2} - \hat{u}_{i,j-1/2} \end{aligned} \quad (13)$$

At the boundary of the SV, the solution is discontinuous. We have to determine the numerical flux $f_{i,1/2}$ in terms of its left state and right state, namely,

$$f_{i-1,k+1/2} = f_{i,1/2} = f(u_{i-1,k+1/2}, u_{i,1/2}) \quad (14)$$

Numerical method developed in finite volume method, such as approximated Riemann solver, can be applied for this purpose. For the scalar equation investigated in the present study, upwind scheme is applied to compute the numerical flux $f_{i,j+1/2}$. The computation of the numerical flux $\hat{q}$ and $\hat{u}$ is specific to the local SV formulation. They are chosen according to [16].

$$\begin{aligned} \hat{u}_{i,1/2} &= u_{i,1/2} \\ \hat{q}_{i,1/2} &= q_{i-1,k+1/2} \end{aligned} \quad (15)$$

The selection of upwind/downwind for u and q can be choosen alternatively. Third-order TVD Runge-Kutta method [5] is applied for time integration. Let k be the degree of the reconstruction polynomial. Numerical solutions are computed at $t = 0.7$ for the five cases:$k = 1$ (linear reconstruction),$k = 2$(quadratic reconstruction), $k = 3$(cubic reconstruction), $k = 4$ (quartic reconstruction), and $k = 5$ (quintic reconstruction). The L1 and L_∞ errors and observed orders of accuracy are presented in the comparison tables and graghs, from which we note that a $(k+1)^{th}$ order of accuracy is achieved for a degree m polynomial reconstruction. No discontinuity is present at the internal interfaces of the CV inside a SV. At these internal interfaces, numerical flux are computed directly using the reconstruction function.

4. SYMMETRY PRESERVATION IN SPECTRAL VOLUME (SPSV) METHOD

In the SPSV formulation, equation (1) is directly interaged over each CV, which gives:

$$u_{i,j}(t).h_{i,j} + [f_{i,j+1/2} - f_{i,j-1/2}] = \mu\left[\frac{du}{dx}|_{i,j+1/2} - \frac{du}{dx}|_{i,j-1/2}\right] \quad (16)$$

Solution unknowns and the fluxes are computed using two sets of points, i.e., solution points and flux points. Figure 1 depics these two sets of points. The conserved variables at the solution points represent the solution unknown. Whereas, the fluxes are computed at the flux points in order to update the solution unknowns. With k solution unknowns, a polynomial of $(k-1)$ degree can be reconstructed.

For our case, the flux points are given as:

$$x_{i+1/2} = \frac{i*[b-a]}{k*N}, \quad i = 0,1,,,k \quad (17)$$

Whereas solution points are given as:

$$x_i^c = \frac{1}{2}(x_{i+1/2} + x_{i-1/2}), \quad i = 1,2,,,k \quad (18)$$

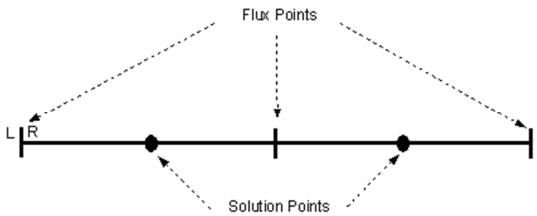

Fig. 1: Linear Spectral Volume

Based on the solution unknowns at the solution points, the solution in the spectral volume is reconstructed with a $(k-1)$ degree Lagrange interpolation polynomial given by,

$$h_j(x) = \prod_{s=1_{s\neq j}}^{k} \{\frac{x-x_s}{x_j-x_s}\} \quad (19)$$

This reconstruction function is referred to as the primary reconstruction function. To compute the viscous flux, we construct a new k degree Lagrange polynomial based on the conserved variables at the flux points.

$$l_{j+1/2}(x) = \prod_{\substack{s=0 \\ s\neq j}}^{N} \left\{\frac{x - x_{s+1/2}}{x_{j+1/2} - x_{s+1/2}}\right\} \quad (20)$$

This new reconstruction function is reffered to as auxilary reconstruction function. The idea of using an auxilary reconstruction function was first proposed in [21] for a staggered-grid multi-domain spectral method and adapted by Wang et al. in a spectral difference method [22].

The following steps are used to compute the inviscid flux:

1. Given the cell-averaged value $\bar{u}_i$ for conserved variable for each control volume, conserved variables at the flux points are computed using equation (9).
2. The inviscid fluxes are computed directly using the flux function because the solution is continuous.
3. The inviscid fluxesare computed at the spectral volume interfaces based on the left and the right states using an appropriate flux reconstruction scheme such as a Riemann solver. As we consider a scalar equation here, an upwinding scheme without limiter is applied.

The computation of viscous flux comprises the following steps.

1. The conserved variables at the flux points are computed using the primary reconstruction function.
2. The solutions at both sides of the SV interface are used to compute the average solution, i.e.,

$$\bar{u} = \frac{1}{2}(u_L + u_R)$$

The solution is updated at the boundary of the computational domain with boundary condition. Then, the auxilary reconstruction function is computed.

3. The gradient at the cell interface flux points is computed using the average of the gradients at both sides of the SV interface, i.e.,

$$\nabla\bar{u} = \frac{1}{2}(\nabla\bar{u}_L + \nabla\bar{u}_R)$$

Here, the gradients on both sides of the interface are computed with the auxilary reconstruction function.

At internal interface (control volume interface inside the SV) two choices are possible.

1. $u_x|_{i,j+1/2}, \quad j = 1,2,\ldots,k-1$ computed with the auxilary reconstruction function. This is reffered to as A-Scheme.
2. $u_x|_{i,j+1/2}, \quad j = 1,2,\ldots,k-1$ computed with the primary reconstruction function. This is referred to as P-Scheme.

In persuance of higher accuracy, we apply A-scheme for odd order and P-scheme for even order.

5. NUMERICAL EVALUATION

We apply the proposed technique on diffusion equation and Burger's equation.

5.1. Diffusion Equation

Let us consider one-dimensional diffusion equation,

$$u_t = u_{xx}, \qquad x \in [0,2\pi] \quad (21)$$

with initial conditions $u(x,0) = \sin(x)$. The numerical analysis for every formulation is performed with periodic and Dirichlet boundary conditions. The exact solution of diffusion equation is given as under.

$$u(x,t) = e^{-t}\sin(x)$$

We perform a number of tests in order to evaluate these two mentioned formulations. The results of these tests are described explicitly under different headings.

5.1.1. Symmetry Problem

Diffusion equation contains the elliptical operator and other numerical methods lose symmetry when solving such type of equations. A numerical method must have the symmetry conserving property to achieve good accuracy. To check out the symmetry of the schemes, we select a third order SV method as a reference case. The domain is divided into 40 grid points. The comparison of these formulations is made with the exact solution. For simplicity, the results of first three and last two points are given in Table 1 and Table 2. It is evident that for both boundary conditions, only SPSV preserves the anti-symmetry features of the exact solution.

Table 1: Comparison with periodic boundary conditions

x	Exact Solution	SPSV Formulation	Local SV Formulation
0.026179	0.0130004	0.0129884	0.0129826
0.078539	0.0389656	0.0389656	0.0389775
0.130899	0.0648240	0.0648358	0.0648300
6.204645	-0.0389656	-0.0389656	-0.0389538
6.257005	-0.0130004	-0.0129884	-0.0129945

Table 2: Comparison with Dirichlet boundary conditions

x	Exact Solution	SPSV Formulation	Local SV Formulation
0.026179	0.0130004	0.0129884	0.0129737
0.078539	0.0389656	0.0389656	0.0389687
0.130899	0.0648240	0.0648358	0.0648213
6.204645	-0.0389656	-0.0389656	-0.0389746
6.257005	-0.0130004	-0.0129884	-0.0129435

The results given in Table 1 and Table 2 clearly show that the SPSV formulation preserves the anti-symmetry feature of the exact solution with both types of boundary condition.

5.1.2. Accuracy Analysis

Space discretization uptil sixth order is done for the presented formulations. OASP formulation with the optimalaccuracy condition is used here. Courant-Friedrich-Levy (CFL) number is chosen as high as possible for each order of discretization. Instead of all the results only L1 error for periodic boundary condition and L1 error for Dirichlet boundary condition with their respective achieved order are presented. To check the accuracy, SPSV formulation with optimal accuracy condition is compared with the local SV formulation. The accuracy up to 3rd order with different CFL and boundary conditions is presented in Table 3-6.

Table 3: 2nd order linear SV with CFL=0.6 (periodic boundary condition)

	Local SV Formulation				SPSV Formulation			
H	L1 Eerror	L1 Order	L_∞error	L_∞order	L1 Eerror	L1 Order	L_∞error	L_∞order
10	8.36E-3		2.29E-2		6.22E-3		9.82E-3	
20	1.99E-3	2.065	5.91E-3	1.9561	1.73E-3	1.843	2.72E-3	1.852
40	4.90E-4	2.0248	1.47E-3	1.998	4.49E-4	1.949	7.05E-4	1.947
80	1.22E-4	2.007	3.70E-4	1.999	1.13E-4	1.986	1.78E-4	1.986
160	3.04E-5	2.001	9.25E-5	1.999	2.84E-5	1.996	4.46E-5	1.996
320	7.61E-6	2.000	2.31E-5	1.999	7.10E-6	1.999	1.11E-5	1.999

Table 4: 3rd order quadtratic SVwith CFL=0.4 (periodic boundary condition)

	Local SV Formulation				SPSV Formulation			
H	L1 Eerror	L1 Order	L_∞error	L_∞order	L1 Eerror	L1 Order	L_∞error	L_∞order
10	4.93E-4		1.15E-3		3.90E-4		8.60E-4	
20	6.09E-5	3.0163	1.42E-4	3.011	4.26E-5	3.195	9.78E-5	3.136
40	7.57E-6	3.008	1.78E-5	3.000	5.14E-6	3.049	1.19E-5	3.031
80	9.45E-7	3.002	2.22E-6	3.000	6.35E-7	3.017	1.48E-6	3.007
160	1.18E-7	3.000	2.78E-7	3.000	7.90E-8	3.006	1.85E-7	3.001
320	1.47E-8	3.000	3.48E-8	2.999	9.86E-9	3.002	2.32E-8	3.000

Table 5: 2nd order linear SVwith CFL=0.6(Dirichlet boundary condition)

	Local SV Formulation				SPSV Formulation			
H	L1 Eerror	L1 Order	L_∞error	L_∞order	L1 Eerror	L1 Order	L_∞error	L_∞order
10	1.52E-2		7.58E-2		6.22E-3		9.82E-3	
20	3.91E-3	1.967	3.92E-2	0.949	1.73E-3	1.843	2.72E-3	1.852
40	9.81E-4	1.994	1.97E-2	0.991	4.49E-4	1.949	7.05E-4	1.947
80	2.45E-4	1.999	9.88E-3	0.998	1.13E-4	1.986	1.78E-4	1.986
160	6.13E-5	1.999	4.94E-3	0.999	2.84E-5	1.996	4.46E-5	1.996
320	1.53E-5	1.999	2.47E-3	0.999	7.10E-6	1.999	1.11E-5	1.999

Table 6: 3rd order quadratic SV with CFL=0.5 (Dirichlet boundary condition)

	Local SV Formulation				SPSV Formulation			
H	L1 Eerror	L1 Order	L_∞error	L_∞order	L1 Eerror	L1 Order	L_∞error	L_∞order
10	6.63E-4		3.49E-3		3.90E-4		8.60E-4	
20	7.04E-5	3.234	4.52E-4	2.952	4.26E-5	3.195	9.78E-5	3.136
40	8.16E-6	3.108	5.69E-5	2.989	5.14E-6	3.049	1.19E-5	3.031
80	9.82E-7	3.055	7.12E-6	2.997	6.35E-7	3.017	1.48E-6	3.007
160	1.20E-7	3.026	8.91E-7	2.999	7.90E-8	3.006	1.85E-7	3.001
320	1.49E-8	3.013	1.11E-7	2.999	9.86E-9	3.002	2.32E-8	3.000

From our numerical results, it is clear that the accuracy of the local SV formulation depends on the boundary conditions. For periodic boundary condition,$(k+1)$th order is achieved for k degree polynomial. Whereas, for Dirichlet boundary condition, $(k+1)$th order for L1 can be achieved. However, for L_∞ norm, it is not same for even and odd order. For even order, k^{th} order is achieved and for odd order, $(k+1)$th order is observed. Hence, we can conclude that with periodic boundary condition, only odd order SPSV formulation is more accurate than odd order local SV formulation. Whereas, for Dirichlet boundary condition, SPSV formulation is found to be more accurate than local SV formulation for all orders.

5.1.3. Stabilty Issue

Explicit scheme works well for quite small CFL number as compared to the implicit scheme. As we increse the the CFL number for an explicit scheme, its stability increases. We perform the numerical tests with varying CFL to check the respective stability of the formulations. The variation of maximum allowable CFL number versus the order of accuracy is shown in Figure 2.

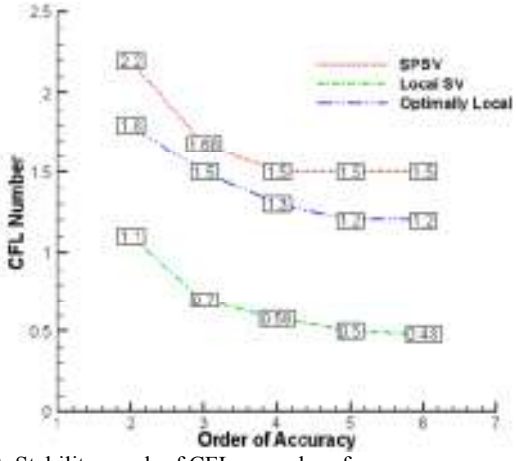

Fig. 2: Stability gragh of CFL vs. order of accuracy

Each formulation has almost the same behaviour for stabilty, but not the same value. From Figure 2, local SV formulation achieves stability at very small CFL number. Whereas, other formulations have relatively high threshold for the CFL number. Among them OASP formulation have high value of CFL number at the same respective order of accuracy and is the most stable among of the other formulations.

5.2. Burger Equation

Let us now consider one-dimansional Burger equation with implicit method, given by,

$$u_t + uu_x = \mu u_{xx}, \qquad x \in [0,1] \tag{22}$$

with initial condition $u(x,0) = 0$ and the boundary conditions $u(0,t) = 0$, $u(1,t) = -\tanh(\frac{1}{2\mu})$.

The problem has following exact steady solution,

$$u(x,t) = -\tanh(\frac{x}{2\mu}) \tag{23}$$

where $\mu = 0.1$. The simulation is run untill the convergence is achieved by using the implicit method. The convergence criterion is residuals $\leq 10^{-12}$ and the difference between two successive iterations is 10^{-15}. Deferred correction implicit method [23] is applied to achieve the numerical solution for SV method. Numerical results for the viscous Burger are given in Table 13-15.

The numerical results show that the local SV formulation is able to achieve $(k+1)$th order for k degree polynomial. Unlike diffusion equation, we observe even order for Burger equation. The reason for this behavior is the following. For diffusion equation, we observe the error on the left side and for Burger equation left hand side is almost the same. Therefore, no such behavior is observed. However, if we change the convection direction, the effects may be prominent.

Table 13: 2nd order linear SV

	Local SV Formulation				SPSV Formulation			
H	**L1 Error**	**L1 Order**	**L_∞Error**	**L_∞Order**	**L1 Error**	**L1 Order**	**L_∞Error**	**L_∞Order**
10	3.67E-4		3.08E-3		2.88E-4		3.79E-3	
20	4.00E-5	3.196	4.21E-4	2.874	2.47E-5	3.541	2.47E-4	3.941
40	4.93E-6	3.020	5.38E-5	2.968	2.99E-6	3.044	2.58E-5	3.258
80	6.19E-7	2.995	6.76E-6	2.991	3.77E-7	2.987	3.08E-6	3.067
160	7.76E-8	2.995	8.47E-7	2.997	4.75E-8	2.989	3.79E-7	3.020
320	9.72E-9	2.996	1.05E-7	2.999	5.98E-9	2.991	4.72E-8	3.6
640	1.29E-9	2.912	1.37E-8	2.949	7.74E-010	2.948	5.89E-9	3.002

Table 14: 3rd order quadratic SV

	Local SV Formulation				SPSV Formulation			
H	**L1 Error**	**L1 Order**	**L_∞Error**	**L_∞Order**	**L1 Error**	**L1 Order**	**L_∞Error**	**L_∞Order**
10	2.37E-3		2.00E-2		2.13E-3		6.65E-3	
20	7.03E-4	1.755	5.63E-3	1.829	8.08E-4	1.645	2.12E-3	1.397
40	1.94E-4	1.856	1.50E-3	1.909	2.43E-4	1.731	6.25E-4	1.765
80	5.11E-5	1.926	3.91E-4	1.938	6.60E-5	1.881	1.64E-4	1.927
160	1.31E-5	1.962	9.97E-5	1.971	1.71E-5	1.944	4.21E-5	1.964
320	3.32E-6	1.980	2.51E-5	1.986	4.36E-6	1.974	1.06E-5	1.979
640	8.36E-7	1.990	6.32E-6	1.993	1.10E-6	1.987	2.68E-6	1.990

6. CONCLUSION

In this paper, we have proposed a novel formulation for the spectral volume method referred to as Symmetry Preservation in Spectral Volume (SPSV) which is able to preserve the symmetry property of the elliptical operator. We implemented the newly proposed formulation on diffusion equation and Burger equation using two different boundary conditions, i.e., periodic and Dirichlet. We set three different criterion to evaluate this formulation: (i) symmetry preserving capability, (ii) accuracy, and (iii) stability. Furthermore, we also presented a detailed comparison between the local SV and the SPSV formulations. We showed that the optimal accuracy can be achieved in L_∞ norm with Dirichlet boundary conditions using SPSV formulation, which is not possible in the local SV formulation. Our comparison results show that the SPSV formulation is more accurate and stable.

REFERENCES

[1] Wang ZJ. Spectral (finite) volume method for conservation laws on unstructured grids: basic formulation. Journal of Computational Physics 2002; 178:210-251.

[2] Wang ZJ, Liu Y. Spectral (finite) volume method for conservation laws on unstructured grids III: one-dimensional systems and partition optimization. Journal of Scientific Computing 2004; 20:137-157.

[3] Wang ZJ, Zhang L, Liu Y. Spectral (finite) volume method for conservation laws on unstructured grids IV: extension to two-dimensional Euler equations. Journal of Computational Physics 2004; 194:716-741.

[4] Cockburn B, Lin S-Y, Shu C-W. TVD Runge-Kutta local projection discontinuous Galerkin finite element method for conservation laws III: one-dimensional systems. Journal of Computational Physics 1989; 84: 90-113.

[5] Zhang M, Shu C-W. An analysis of and a comparison between the discontinuous Galerkin and spectral finite volume methods. Computers and Fluids,2005;34: 581-592.

[6] Sun Y, Wang ZJ. Evaluation of discontinuous Galerkin and spectral volume methods for scalar and system conservation laws on unstructured grids. International Journal for Numerical Methods in Fluids 2004; 45: 819-838.

[7] Barth TJ, Frederickson PO. High-order solution of the Euler equations on unstructured grids using quadratic reconstruction. AIAA Paper No. 90-0013, 1990.

[8] Abgrall, R. (1994). On essentially non-oscillatory schemes on unstructured meshes: analysis and implementation. J. Comp. Phys. 114, 45-58.

[9] Friedrich, O. (1998). Weighted essentially non-oscillatory schemes for the interpolation of mean values on unstructured grids. J. Comp. Phys. 144, 194-212.

[10] Harten, A., Engquist, B., Osher, S., and Chakravarthy, S. (1987). Uniformly high order essentially non-oscillatory schemes III. J. Comp. Phys. 71, 231.

[11] Hu, C., and Shu, C. W. (1999). Weighted essentially non-oscillatory schemes on triangular meshes. J. Comp. Phys. 150, 97-127.

[12] Shu C-W. Essentially non-oscillatory and weighted essentially non-oscillatory schemes for hyperbolic conservation laws. In Advanced Numerical Approximation of Nonlinear Hyperbolic Equations, Cockburn B, Johnson C, Shu C-W, Tadmor E, Quarteroni A (eds). Lecture Notes in Mathematics, vol. 1697. Springer:Berlin,1998; 325-432.

[13] Godunov SK. A finite-difference method for the numerical computation of discontinuous solutions of the equations of uid dynamics. Mathematics of the USSR-Sbornik 1959; 47:271.

[14] Shu C-W, Osher S. Efficient implementation of essentially non-oscillatory shock capturing schemes. Journal of Computational Physics 1988; 77:439-471.

[15] Shu C-W. TVB uniformly high-order schemes for conservation laws. Mathematics of Computation 1987; 49:105-121.

[16] Yuzhi Sun, Z.J. Wang.Formulations and analysis of the spectral volume method for the diffusion equation. Communication in Numerical Methods in Engineering 2004;20:927-937

[17] Cockburn B, Shu C-W. The local discontinuous Galerkin method for time-dependent convection di usion system.SIAM Journal on Numerical Analysis 1998; 35:2440-2463.

[18] Baumann CE, Oden JT. A discontinuous hp finite element method for convection-diffusion problems. Computer Methods in Applied Mechanics and Engineering 1999; 175:311-341.

[19] Oden JT, Babuska I, Baumann CE. A discontinuous hp finite element method for diffusion problems. Journal of Computational Physics 1998; 146:491-519.

[20] Riviere B, Wheeler M, Girault V. A priori error estimates for finite element methods based on discontinuous approximation spaces for elliptic problems. SIAM Journal on Numerical Analysis 2001; 39:902-931.

[21] D.A. Kopriva. A conservation staggered-grid multidomain spectral method for the compressible Navier-Stokes equations. Journal of Computational Physics 1998;143:125-158. 39:902-931.

[22] Y. Sun, Z.J. Wang and Y. Liu. High-order multidomain spectral difference method for the Navier-Stokes equations. AIAA-2006-0301.

[23] Minion, Michael L. Semi-implicit spectral deferred correction methods for ordinary differential equations. Communications in Mathematical Sciences 1.3 (2003): 471-500.

ENHANCED AUTONOMIC NETWORKING MANAGEMENT ARCHITECTURE (ENAMA)

Asif Ali Laghari*, Intesab Hussain Sadhayo**, Muhammad Ibrahim Channa*

ABSTRACT

A Computer Network which automatically configures itself and adopts the services which fulfil user requirements according to their needs is called autonomic network. Autonomic network self manages the services for heterogeneous devices and modify polices for users to satisfy them from network services. In ENhanced Autonomic network Management Architecture (ENAMA), we propose two blocks of processing which control the operations of management as well as for learning from environment and take decisions for network related issues. QoE will be used for collecting data for learning from external environment and store in Long Term Memory (LTM) block for future analysis and decisions. The proposed ENAMA is the fast learning autonomic network management architecture; it will take most accurate decisions to handle the critical situations.

Keywords: *Autonomic Network, Quality of Service (QoS), Quality of Experience (QoE), Policy Based Network, Learning, Decision*

1. INTRODUCTION

The foundation of autonomic network is based on human nervous system and intelligence of the brain. Autonomic network reacts on every action within few seconds, have no fix policy for users, polices and decisions are change on the behalf of users needs. There were different architecture models developed by reported originations like IBM, DARPA and FOCALE ,but these models couldn't work fully like human brain. Therefore, there is a need for new architecture model that work like human brain very intelligently and can learn from environment within short time and make accurate decisions to handle the situation.

In policy based networks, administrator set policies for long time, due to the fix policies, there was problem for connect new devices with network and also there is no permission for using new type of services [1]. Administrator had to do work hard to provide QoS to client and provide access of new services while solving the problems of connectivity with heterogeneous devices with network.

Autonomic network provides many advantages over the manual network. Autonomic network is self-configuration; self-optimization and self-healing. By using these features network manage all resources and take actions or make decisions automatically [8]. The challenges and limitations behind such implementation include the representation of knowledge at the resource management level, unification and simplification of business processes, information technology across the domain, and precise and scalable knowledge base. Systems should have solutions to cover different standards and allowing interoperability between equivalents but heterogeneously instantiated domain knowledge. Existing operators cannot manage the domains and they do not adopt same representation for their managed entities including their properties, relationships and operations.

Autonomic networks reduce the burden from the administrator to automatically configure devices on network. There is no fix policy for the user. The policies are changed on every new request of the user and provide quality of service (QoS) to clients. QoS was used in past by several organizations to improve technological aspect of network devices to fill the user needs, but they didn't succeed at all. In ENAMA, we use QoE which depends on user experience. It measures the QoE from user actions, analyzes their needs on the network and tries to fulfill the user and organization requirements [2]. QoE is all about user perception, feelings, errors and satisfaction at the time when he uses particular service or product. QoE data is analyzed to extract their experience about the services and this data provides help to administrators for improving the technological aspects for the betterment of QoS for end users [9].

In ENAMA (ENhanced Autonomic Network Management Architecture), we propose new monitoring idea for learning and decisions which are based on human learning and decision ability. Fact is that human beings learning ability depends on trying different experiments and by keeping focus on environment and surroundings entities then finally

* Department of Information Technology

** Department of computer systems engineering

Quaid-e-Awam University of Engineering Science & Technology, Nawabshah Sindh Pakistan

asifalilaghari@hotmail.com, intesab, Ibrahim.channa@{quest.edu.pk}

they made accurate decision for the solution of problem. In old ideas predefined techniques were used for monitoring or fix policies, so monitoring section monitors environment within the limited scope and blocked the new services and process for execution. If any authorized user will launch the attack or attach malicious type process then the system fails to respond. In our proposed model we use two processing units, one active doing processing and other for backup and this model allows processes for once execution. In ENAMA model, two processing blocks working same like left right brain functionality of human beings, left side of brain used for learning skills and right of brain is used for creation of innovation also for holistic thoughts [3, 4].

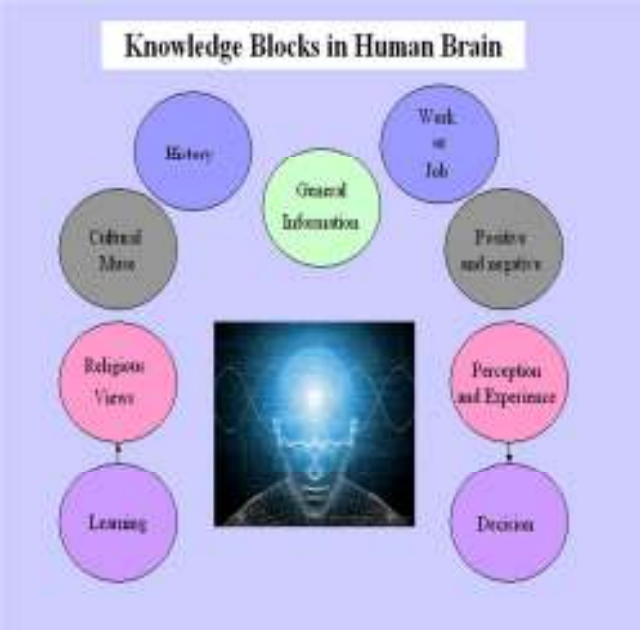

Fig 1. Knowledge Representation in Human Brain

2. RELATED WORK

The architecture of autonomic network was given by different researchers and organizations such as IBM, DARPA (Defense Advanced Research Project Agency) FOCALE architecture, Cognitive Network, Bionet project from NSF (National Science Foundation).

Autonomic network is combination of highly heterogeneous distributed systems, which depend on set autonomic entities (AE). Every entity is a set of managed resources, services and offers services to user or peer autonomic network. The architecture of autonomic components require abilities to allow every entity to analyze the behavior of local processing and also monitor the environment and react on event, configure itself on the basis of data which was collected from the other entities. Communication between the entities and components in the network environment provide collective intelligence to achieve the goal.

This IBM Autonomic element architecture model is composed of different modules that enable the expected autonomic behaviors through the set of autonomic operations can achieve by using self adjusting control loop. [6] Control loop depends on components of system, every component transfers signal to other components with policy driven management rules for controlling the system operations. The outputs of components are sent because autobody panels' emphasis curved surface whole artistic effects, measurement accuracy is not the first problem considered in the course of the measuring car body, but trying to make the development time shorter [4]. Signal to system for adjust the operations according to messages given by the autonomic elements [1, 6].

The control module introduces two types of components called sensors and effectors. Sensors collect data from environment and effectors allow the configuration of its managed resources. Autonomic entity of monitoring module collects data using different techniques, aggregates, filter and manage information collected by sensors from environment. All information goes to analyze phase that analyze the information of environment and make plan to control the components. Then loop moves to execute module that executes the plan, performs set of specified actions. Once the goal is specified, the interaction workflow between different modules and allows the router to behave in autonomic manner without administrator interaction. There are two level of control over managed resources and autonomic entity. The control loop of autonomic entity allows immediate action to modify in the autonomic entity to be imposed another general loop called global control loop aspire to impose a automatic behavior of the autonomic entity as regards more compulsory condition changes in its surrounding environment. [1].

2.1 Cognitive Network DARPA

In this approach there is main focus on the cognitive capabilities of future network architecture. [7] The aim of cognitive network architecture is to produce cognitive process of human computational model. Cognitive architecture should not be implemented partly but it needs complete implementation of various aspects of cognitive behavior as well as complete system. The aim of architecture is to reproduce the action on the basis of short term and long term and also learn from previous execution. These cognitive aspects are aligned with IBM approach but they differ in terminology and definitions DARPA proposed three processes related to cognitive behaviors; reactive, deliberative and reflective reason process. It is same like IBM and FOCALE architecture.

The reactive processes get information from environment automatically and react on that information by storing information for future. Deliberative process analyzes compares and evaluates the situation and the reflective process monitors and controls failure behavior response to previous performance by using cognitive element and execution history for decisions.

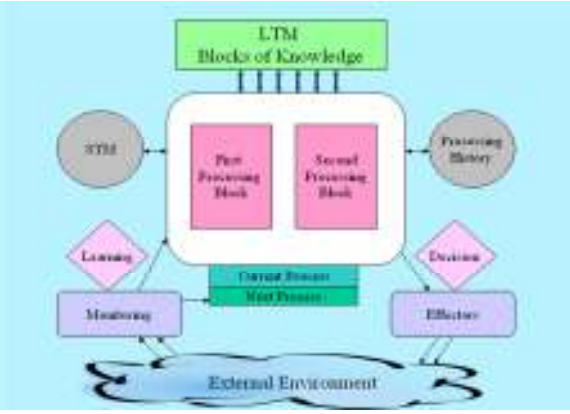

Fig 2. Enhanced Autonomic Network Management Architecture (ENAMA)

2.2 Bio-Networking Architecture

This architecture was developed with Bionet project at the University of California, Ervine and supported by NSF and DARPA. This architecture is like biological system to scale, adopt and survive automatically [5, 7]. In this architecture, cyber entities are used as autonomous mobile agent to implement network system. The Bio-Networking approach relies on mobile agent's background and reuse its concepts but it's not clear today whether autonomic network should relay on mobile agent or not. [1, 7]

2.3 FOCALE Architecture

FOCALE (Foundation, Observation, Comparison, Action and Learning Environment) was introduced by Motorola in collaboration with the LRSM lab of the University of Evry and TSSG Lab.

In this architecture, managed resources can be turned into an autonomic component. Autonomic Computing Element (ACE) is used to manage resource and functionality throughout the system [6, 7].

The ENAMA architectures have different features compare to other autonomic network architectures and comparison is given in table 1. Automatic policy change is also feature of this architecture which is given in EQoM framework [14].

For automatic policy ,the network architecture collect data of every user from network and compare that data of user with user default policy, if user can't services according to SLA than it upgrades the services for particular user and provide quality of service to end users.

3. ENAMA ARCHITECTURE

ENAMA system will work by monitoring the network environment and collect data about network services,

devices and also QoE data of user. This data will be stored in LTM blocks for future usage. The purpose of adding QoE domain is to act like human beings as they get experience from conversation with different people in different situations, behaviors and attitude to make human more knowledgeable to make decision. QoE is involved to obtain users needs, service usage level of expertise because system update database of LTM block according to user behavior and respond them according to their requests otherwise system will not be more intelligent it's decision making ability will not satisfy the user.

ENAMA will learn from environment by agent based framework, agents run from server to client and monitoring network by collecting information of network devices like switches, routers their status and about heterogeneous nodes which are connected with network. Components of ENAMA (Enhanced Autonomic Network Management architecture) are given in figure 2.

Table 1. Comparison of Enama with other Autonomic Architectures

Autonomic Architectures	IBM [10]	FOCALE [11]	Bionet [12]	Cognitive Architecture [13]	ENAMA
QoE Support	No	No	No	No	Yes
Learning ability from new process	Limited	Limited	Limited	Limited	Advance
Action on Malicious or new type of process	Access prevent	Access prevent	Access prevent	Access prevent	Allow access and damage control ability
Human Brain Architectures support	Yes	Yes	Yes	Yes	Advance
Policy change according user needs	No	No	No	No	Yes

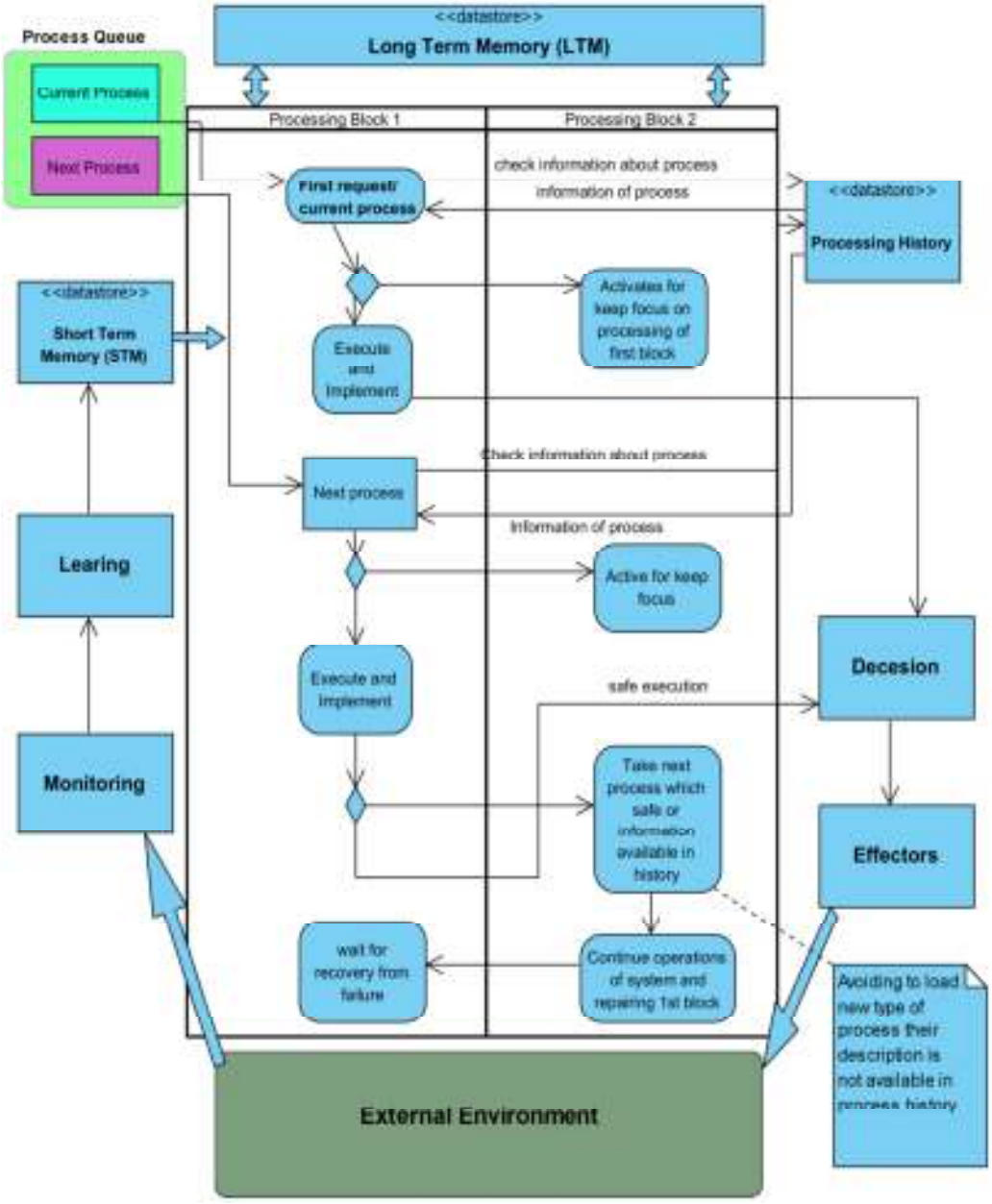

Fig 3. Activity Diagram of Enhanced Autonomic Network Management Architecture (ENAMA)

4. ACTIVITY DIAGRAM OF ENAMA

The activity diagram explains how two processor blocks executes processes in ENAMA architecture. We present execution actives of two processes.

- Processor blocks are connected with Short Term Memory (STM), which contains current data monitored from network and data of system. Long Term Memory (LTM) permanent storage which contains operating system, and other data which support for execution of process. System load a process from process queue for execution in first block, first processor block get information about process from process history, if information available about process then decision node move to executes and implement and send executed data to decision phase to apply new rules. If not then it activates the 2nd processor block for keeping eyes

and ready for controlling operation of system when first processor block goes down.

- System loads new process from process queue for execution, processor block get information from about process from process history, if information is not available about process. For new type of processes, 2nd processor block activates for keeping track of system operations and first processor block attempt to execution of process. After successful execution of process, decision node send information to decision phase, if first processor blocks fails in execution due to malicious type process then decision node transfer control to 2nd processor block to control the rest of operations of system for execution in future. In next action, 2nd processor block executes safe processes or those processes their information is already available in information history and also starts action for recovery of first processor block from failure.

5. CONCLUSION

We proposed ENAMA model based on human brain intelligence having different knowledge blocks in the mind to answer the queries and ability to take most accurate decisions according to situation. In this paper, we discussed about left right functions which help us to learn and make decisions. The same idea imposed in ENAMA model with two units of processing interconnected to adopt functionalities of learning and decision making. In the ENAMA, QoE helps to analyze the user way of using services that helps ENAMA to answer the queries of user accurately using LTM block.

In future development of hardware framework according to proposed architecture and software developer mostly open source operating system developer will try to make functionality of operating system according to proposed architecture then it will be better for service provider to satisfy users.

6. ACKNOWLEDGMENT

Authors are thankful to Mr. Muhammad Yousuf Laghari Lecturer in Zoology department in Sindh Muslim College Hyderabad Pakistan to provide us information of human brain functionality in the design of ENAMA Model.

REFERENCES

[1] N Agoulmine, “Autonomic Network management principles from concepts to Applications”, Academic Press, 2012.

[2] Khalil Ur Rehman Laghari, N. Crespi.; Molina, B.; Palau, C.E. ,"QoE Aware Service Delivery in Distributed Environment," Advanced Information Networking and Applications (WAINA), IEEE Workshops of International Conference on , pp.837-842, 2011.

[3] http://frank.mtsu.edu/~studskl/hd/hemis.html

[4] http://www.myshrink.com/left-right-brain-function.php

[5] W. Greene, & B. Lancaster, “Autonomic Networks-Autonomic Communication” LTC International Article for Pipeline Magazine, 2007.

[6] S van der Meer, W. Donnelly, J. Strassner, B. Jennings, M. O. Foghlu, “Emerging principles of Autonomic Network Management”, MACE’06, Vol. 2, No. 1, pp. 29-48, 2006.

[7] S. Balasubramaniam, J. Strassner, N. Agoulmine, D. Botvitch, E. Lehtihet, W. Donnely, “Challenges to Autonomic Network Management”, First conference on Modeling Autonomic communication Environment (MACE’06), Dublin, Ireland, 2006.

[8] M. Liinasuo, I. Aaltonen, H. Karvonen, B. Fuentes, A. Castro, “Human operator perspective to autonomic network management”, Fifth International Conference on Advances in Computer-Human Interactions, pp. 128-134, 2012.

[9] Khalil Ur Rehman Laghari, IGB Yahya, N Crespi, “Towards a Service Delivery Based on Customer experience Ontology: Shift from Service to experience”, Springer-Verlag Berlin Heidelberg , pp. 51-61, 2010.

[10] Y Cheng, R Farha, MS Kim, A Leon-Garcia, J. Won-ki Hong, "A generic architecture for autonomic service and network management." Computer Communications, vol. 29, no. 18, pp. 3691-3709, 2006.

[11] F. De Pellegrini, D. Linner, L. Bacsardi, C. Moiso, "Bionets architecture: from networks to serworks." Bio-Inspired Models of Network, Information and Computing Systems, vol. 2, pp. 255-262, 2007.

[12] J. Strassner, N. Agoulmine, E. Lehtihet, "Focale: A novel autonomic networking architecture.", 2006.

[13] J. Mitola, "Cognitive radio architecture evolution", Proceedings of the IEEE, vol. 97, no. 4, pp. 626-641, 2009.

[14] A. A. Laghari, M. I . Channa, K. R. Laghari, M. Aman, M. Memon, “EQOM: Enhanced Quality of Experience (QoE) Framework for Multimedia Services”, UACEE International Journal of Computer Science and its Applications , vol. 3, no. 1, pp 85-89, 2013.

DESIGN OF A SLOW SAND BED FILTRATION SYSTEM FOR PURIFICATION OF CANAL WATER

Saleem Raza Samo*, Abdul Rehman Jatoi*, Fareed Hussain Mangi*,
Abdul Nasir Laghari*, Kishan Chand Mukwana*

ABSTRACT

The purpose of the present study is to present the design of a filtration system for removal of canal water impurities. The canal water characteristics were examined before and after the treatment with a slow sand bed filtration system. The gravel and sand were used as media for the proposed filtration method. The canal water was introduced in batch wise from the top of the system. The water then passed through the layers of media and purified. The filtered and purified water was collected at the bottom of the system through riser pipe. The pH, turbidity, total dissolved solids (TDS) and electrical conductivity (EC) of canal and filtered water was examined. It is found from the study that the maximum efficiency of the proposed system was 99% in reducing turbidity level and 6% in reducing TDS and EC level. The proposed system was found to be more effective for reducing turbidity from the canal waters among examined parameters.

Keywords: *Canal water, characteristics of water, impurities, media filtration*

1. INTRODUCTION

Water is one of the most important substances and essential natural resource for sustaining the life on earth [1-2]. It can be used for variety of purposes like drinking, cooking, washing, cleaning, agriculture, and industrial development, and growth of plants. The water used for drinking purpose should be safe and clean [3-5]. The majority of population is consuming ground water and surface water for drinking purpose in Pakistan [6]. Since, the quality of surface water is being affected by anthropogenic activities such as urban development, municipal and industrial wastewater discharges, agricultural practices and by natural processes like weathering, sediment transport and soil erosion [7-10]. The anthropogenic activities are the major cause of water quality degradation, however, these activities can be controlled by means of applying better management system and through the usage of different techniques namely physical (settling), chemical (disinfection or coagulation) or biological (slow sand filtration or activated sludge techniques) [11-12]. Besides, it is reported that almost 80 % of ailments and more than 33 % of death are due to the consumption of polluted water in developing countries [13]. Pakistan ranks at number 80 among 122 nations regarding drinking water quality [14-15]. Moreover, the major part of the rural population of Pakistan survives only on the groundwater sources due to unavailability of water treatment systems. It is reported that around 40% deaths are attributed to direct or indirect effect of waterborne diseases in Pakistan [16]. It is because 2000 million gallons per day of sewage is being discharged to the surface water bodies in Pakistan [17-18]. It is further reported that only 6 persons out of 10 have access to safe drinking water in Pakistan [19]. The government has set a target to provide safe drinking water up to 93% of the population by 2015 and to the entire population by 2025 [20-21]. However, it is a very challenging task to achieve the target because of many problems including technical, economic and political barriers.

In this regard, the contribution of research organizations and involvement of every citizen is of prime importance. Therefore, it is our duty to give practical and economical solutions to the government for implementation of projects to achieve the above mentioned goals. Therefore, this study was conducted to develop a cheap and clean filtration technique to remove suspended particulates from the canal waters.

2. MATERIAL AND METHODS

2.1 Study Area

The Gajra wah canal water was selected for this study. The canal is passes through the centre of Nawabshah city and receives the sewage waste from the various locations of the city as well as effluents from Habib Sugar Mills [16, 22]. The maximum quantity of this canal water is being utilized for the irrigation purpose of the area and drinking purpose for the surrounding people. Gajra wah canal is the main source to provide water for drinking and irrigation purpose in the city and surrounding "taluka" Nawabshah. Therefore the quality of Gajra wah canal waters was investigated. The main surface water quality parameters viz. pH, turbidity, total dissolved solids and electrical conductivity were studied. The pH refers to the measurement of hydrogen ion activity in the solution. It is measured on a scale of 0 to 14. A pH of 7 is considered as neutral, above 7 basic and below 7 acidic. Turbidity is a

* Energy & Environment Engineering Department,
Quaid-e-Awam University of Engineering, Science and Technology (QUEST), Nawabshah

measure of water clarity. The material suspended in water decreases the passage of light through the water hence it become opaque. Total dissolved solids (TDS) are a measure of the combined content of all inorganic and organic substances contained in a water sample. Electrical conductivity measures a material's ability to conduct an electric current. The above parameters can indicate the either the water is suitable or not for drinking purpose [23].

2.2 Sample Collection

Ten different locations on Gajra wah canal were selected for investigation of canal water. The samples were taken during the months of July, August and September 2014. Following the grab water sampling method, water samples were collected at varying depths from the surface of the canal and stowed in fresh polythene plastic bottles with a capacity of 1.0 litter each. Three different samples were taken from the same spot for consideration of average values. The samples were stored in thermoset container at 25°C and then analyzed [24].

2.3 Development of Slow Sand Bed Filtration System

Different filtration systems such as rapid sand filtration, slow sand filtration and continuous sand filtration techniques are exist for treatment of canal waters. In rapid sand filtration, there is chance of materials erosion and continuous systems require pressure to push the water through the pores of the media. Since, the slow bed system does not require any force to drive the water through the media and there is also no chance of sand erosion. Therefore, a slow sand bed filtration System (SSBFS) was designed and fabricated in the Department of Energy and Environment Engineering, Quaid-e-Awam University of Engineering Science & Technology (QUEST), Nawabshah, Sindh, Pakistan.

The different components of the designed system are illustrated in Fig. 1. The designed slow sand bed filtration system (SSBFS) comprises of a steel container (763.5 mm in height, 458.1 mm in width & length), screen, lid plate, diffuser plate and a riser pipe. The steel container was used to hold the sand and gravel. A diffuser plate was employed to sprinkle the poured water in a proper way. Small holes were arranged (3 mm in diameter at 25 mm x 25 mm) in a grid pattern. It was fitted at the inlet point of treatment unit. A riser pipe (drain pipe) with small holes was fitted above 50.9 mm from bottom of unit to receive clean water and drain in the clean tub or bottle. Initially riser pipe was wrapped with filtering cloth then fitted in the filter container. The top side of SSBFS was covered with a lid (top cover), which was made from the metallic sheet.

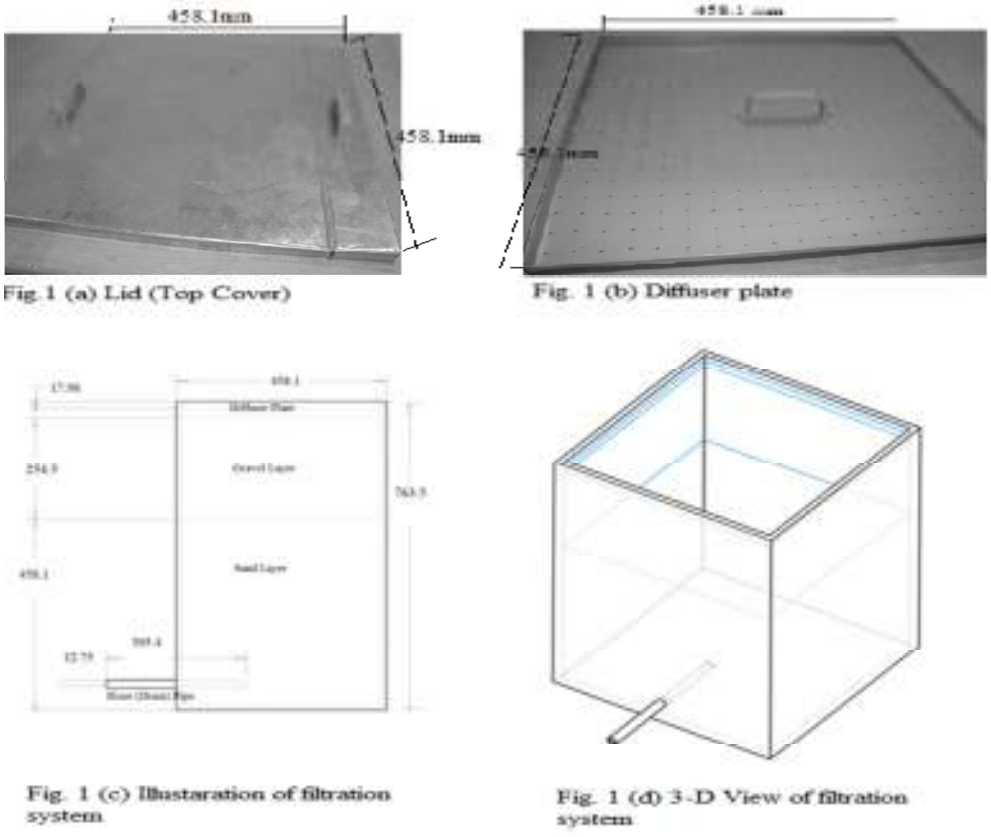

Fig. 1 (a) Lid (Top Cover)

Fig. 1 (b) Diffuser plate

Fig. 1 (c) Illustaration of filtration system

Fig. 1 (d) 3-D View of filtration system

Fig. 1. 3 D view showing different components of proposed filtration system

The purpose of lid was to control the debris, insects and biological reaction inside of treatment system. The cleaned and washed fine sand (0.063- 0.2 mm) and gravel (4.75–12.0 mm) were charged in SSBF system. During the charging of different filtration media's, the 254.5 mm of gravel bed and 458.1 mm of sand layer were provided in the steel container [12, 25-29]. After fabrication of whole system, the water samples were poured from the top of the system through sprinkling technique. The water then passed through the media, where the dissolved solids and turbid materials of the samples were trapped. The filtered water is collected in a clean bottle at the bottom of the designed system.

The selected properties of canal water and filtered water samples namely pH, turbidity, total dissolved solids and electrical conductivity was examined in the Laboratory. The temperature of water samples was measured with the help of thermometers, pH through Lovibond, Sensodirect pH 110 meter and total dissolved solids with ELE International TDS meter Model HI98302 by HANNA. Whereas, Milliampere meter was used to assess the electrical conductivity and Nephelometer (Turbidimeter) for turbidity of canal water samples [30].

3. RESULTS AND DISCUSSION

A total of four parameters, namely pH, turbidity, total dissolved solids and electrical conductivity of Gajra wah water samples were examined as per American Society for Testing and Materials (ASTM). The pH of water samples were tested by ASTM D1293-12, turbidity ASTM D7315-12, total dissolved solids ASTM D5907-13 and electrical conductivity ASTM D1125-14 methods [31].

The average pH value of untreated canal water samples was 8.43, and the maximum and minimum values were 8.77 and 8.11 respectively as shown in Fig. 2. Likewise, the average pH value of treated canal water samples was 7.9, and the maximum and minimum values were 8.17 and 7.69 respectively. It was observed that the pH values of treated water samples were slightly decreased and become closer to the neutral value.

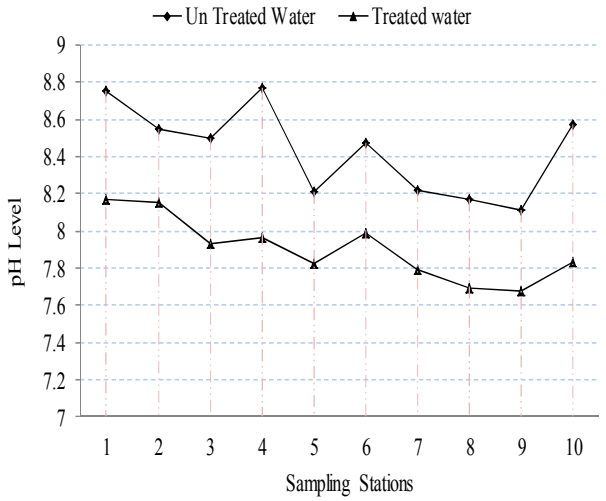

Fig. 2. Results of pH (canal water and treated water samples)

As shown in Fig. 3, the average level of turbidity of untreated canal water samples was 627 FTU with a maximum value of 714 FTU and minimum 557 FTU. Similarly, the average level of turbidity of treated canal water samples was 5.72 FTU with maximum and minimum values of 6.55 FTU and 4.94 FTU respectively. The improvement of turbidity was around 99 %. It is observed from the analysis that turbidity level was successfully improved as compared to other parameters.

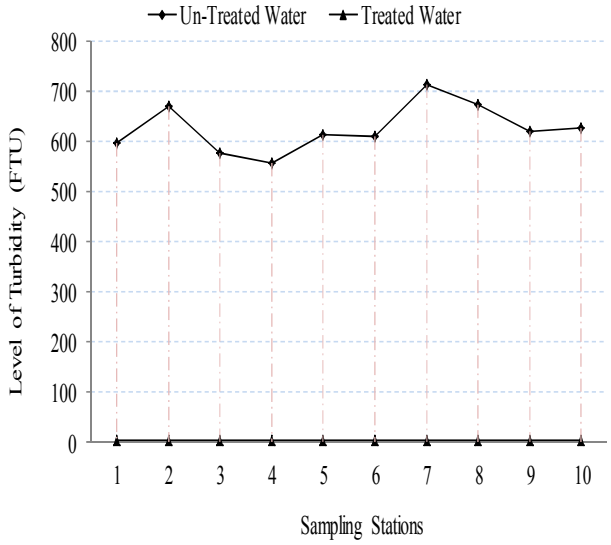

Fig. 3. Results of turbidity (canal water and treated water samples)

The measured results of total dissolved solids (TDS) and electrical conductivity (EC) are shown in Fig. 4. The average level of TDS of untreated canal water samples was 435 mg/l with a maximum and minimum values of 447 mg/l and 415 mg/l respectively. The average TDS value of treated canal water samples was 415 mg/l, and the maximum and minimum values were 427 mg/l and 391 mg/l respectively. The average EC of untreated canal water was 654 µS/cm, and the maximum and minimum values were 672 µS/cm and 625 µS/cm respectively. Likewise, the average EC of treated canal water samples was 621 µS/cm, and the maximum and minimum values were 638 µS/cm and 591 µS/cm respectively. The TDS and EC showed similar behaviour with only 6 % improvement in the examined samples. These both parameters are interrelated with each other, as the increase of TDS results the increase of EC and vice versa.

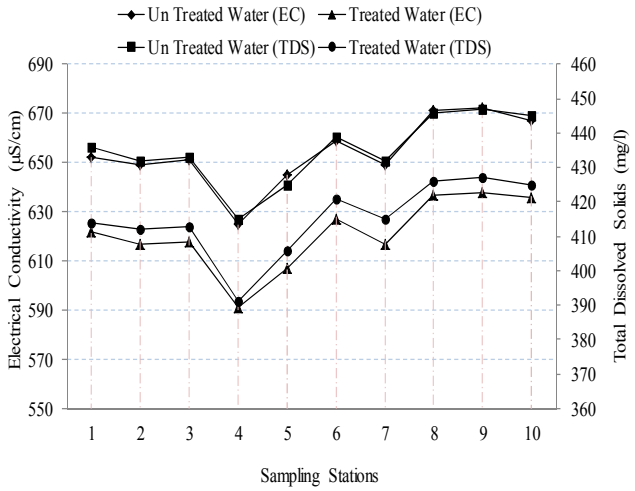

Fig. 4. Results of Electrical conductivity and Total Dissolved Solids (canal water and treated water samples)

4. CONCLUSION AND SUGGESTION

A slow sand bed filtration system is designed and fabricated in the Department of Energy and Environment, Quaid-e-Awam University of Engineering, Science and Technology Nawabshah. The sand and gravel were used as media for the filtration of canal water. The water samples were poured batch wise through sprinkling technique. The pH, turbidity, total dissolved solids and electrical conductivity of canal water and filtered water was analysed. The maximum efficiency of slow sand bed filtration system was found to be 99 % for turbidity and minimum efficiency was 6.28 % for pH. It is observed that the designed system was more effective for removal of turbidity from the canal waters among examined parameters. It is suggested that Sindh Environmental Protection Agency (SEPA) may organize awareness programs for people to prevent the quality of surface and canal waters. SEPA should assure that industries could not throw their effluent directly into the surface water bodies. The random checking of water samples may be carried out in regular intervals (weekly or monthly) to make the quality of drinking waters as per standards.

5. ACKNOWLEDGEMENT

The authors would like to acknowledge the support and help provided by the authorities of Energy and Environment Engineering Department, Quaid-e-Awam University of Engineering Science and Technology, (QUEST), Nawabshah, Pakistan for providing the lab facilities to conduct research.

REFERENCES

[1] Jatoi A.R., Samo S.R. and Jakhrani A.Q., "Analysis of Water Quality: Case Study of Keenjhar Lake, Thatta, Sindh, Pakistan". 6th International Engineering Conference, Energy and Environment, ENCON-2013. ISBN: 978-981-07-6059-5, doi: 10.3850/978-981-07-6059-5_082, available at www.rpsonline.com.sg

[2] Khan, S., Shahnaz, M., Jehan, N., Rehman, S., Shah, M. T., and Din, I., "Drinking water quality and human health risk in Charsadda district, Pakistan", Journal of Cleaner Production, 60, 93-101, 2013.

[3] Rangwala, S. C., Rangwala, K. S., and Rangwala, P. S., "Water supply and sanitary engineering: Environmental Engineering", 1992.

[4] Meenakshi, R.C., "Fluoride in drinking water and its removal", Journal of Hazardous Materials, 137 (1), 456–463, 2006.

[5] Petersen, P. E., "The World Oral Health Report 2003: continuous improvement of oral health in the 21st century–the approach of the WHO Global Oral Health Programme", Community Dentistry and Oral Epidemiology, 31 (1), 3-24, 2003.

[6] Kazi, T. G., Arain, M. B., Jamali, M. K., Jalbani, N., Afridi, H. I., Sarfraz, R. A., and Shah, A. Q., "Assessment of water quality of polluted lake using multivariate statistical techniques: A case study", Ecotoxicology and Environmental Safety, 72 (2), 301-309, 2009.

[7] Shrestha, S., and Kazama, F., "Assessment of surface water quality using multivariate statistical techniques: A case study of the Fuji river basin, Japan", Environmental Modelling & Software, 22 (4), 464-475, 2007.

[8] Midrar-Ul-Haq, Khattak, R. A., Puno, H. K., Saif, M. S and Memon., K. S., "Surface and ground water contamination in NWFP and Sindh provinces with respect to trace elements", International Journal of Agriculture and Biology, 7, 214–217, 2005.

[9] Tariq.M, Ali.M, and Shah. Z., "Characteristics of industrial effluents and their possible impacts on quality of underground water", Soil & Environment, 25, 64–69, 2006.

[10] PCRWR., "Water Quality Status in Rural Areas of Pakistan, Pakistan Council of Research in Water Resources, Islamabad, Pakistan", 2010.

[11] Yousaf, S., Khan, S., Sher, H., Afridi, I., & Ahmad, D., "Canal water treatment with rapid sand filtration", Soil and Environment, 32 (2), 103-107, 2013.

[12] Brikké, F., and Bredero, M., "Linking technology choice with operation and maintenance in the context of community water supply and sanitation. Reference document for planners and project staff. Geneva", WHO and IRC, 2003.

[13] Fahmida, P., Uzma, A., and Usmani, T., "Evaluation of water quality of different colleges of Karachi City" Journal of Chemical Society Pakistan, 29 (5), 458-462, 2007.

[14] Azizullah, A., Khattak, M. N. K., Richter, P., and Häder, D. P., "Water pollution in Pakistan and its impact on public health, A- Review", Environment International, 37 (2), 479-497, 2011.

[15] Rosemann, N., "Drinking Water Crisis in Pakistan and the Issue of Bottled Water: The Case of Nestlé's 'Pure Life", Actionaid Pakistan, 2005.

[16] Khuhawar, M. Y., and Majidano, S. A., "An Investigation of Quality of Groundwater of Taluka Nawabshah", Pakistan Journal of Chemistry, 1 (2), 65-71, 2011.

[17] Aziz, J. A., "Management of source and drinking-water quality in Pakistan", East Mediterranean Health Journal, 11 (5-6), 1087-98, 2005.

[18] SCEA, WB., "Pakistan Strategic Country Environmental Assessment. Main report", Report No. 36946-PK World Bank, 1-66, 2006.

[19] Mahmood, Q., Baig, S. A., Nawab, B., Shafqat, M. N., Pervez, A., and Zeb, B. S., "Development of low cost household drinking water treatment system for the earthquake affected communities in Northern Pakistan", Desalination, 273 (2), 316-320, 2011.

[20] Nawab, B., and Nyborg, I.L.P., "Institutional challenges in water supply and sanitation in Pakistan: revealing the gap between national policy and local experiences", Water Policy, 11 (5), 582–597, 2009.

[21] NDWP. Draft., "National Drinking Water Policy", Ministry of Environment, Government of Pakistan", 2009. (www.environment.gov.pk)

[22] Waseem, A., Arshad, J., Iqbal, F., Sajjad, A., Mehmood, Z., and Murtaza, G., "Pollution Status of Pakistan", A Retrospective Review on Heavy Metal Contamination of Water, Soil and Vegetables. Bio Med Research International, 1-29, 2014.

[23] Baig, J. A., Kazi, T. G., Arain, M. B., Afridi, H. I., Kandhro, G. A., Sarfraz, R. A., and Shah, A. Q., Evaluation of arsenic and other physico-chemical parameters of surface and ground water of Jamshoro, Pakistan. Journal of Hazardous Materials, 166 (2), 662-669, 2009.

[24] Lashari, K.H., Korai, A.L., Sahato, G.A., and Kazi, T.G., "Limnological Studies of Keenjhar Lake", Pakistan Journal of Analytical and Environmental Chemistry, 10 (1-2), 39-47, 2009.

[25] Ahammed, M. M., and Davra, K., "Performance evaluation of biosand filter modified with iron oxide-coated sand for household treatment of drinking water", Desalination, 276 (1), 287-293, 2011.

[26] Ellis, K. V., "Slow sand filtration as a technique for the tertiary treatment of municipal sewages", Water Research, 21(4), 403-410, 1987.

[27] Kohne, R. W., and Logsdon, G. S., "Slow Sand Filtration", Bridging the Gap:, 1-3, 2001.

[28] El-Taweel, G. E., and Ali, G. H., "Evaluation of roughing and slow sand filters for water treatment", Water, Air and Soil Pollution, 120 (1-2), 21-28, 2000.

[29] Helmreich, B., and Horn, H., "Opportunities in rainwater harvesting", Desalination, 248 (1), 118-124, 2009.

[30] Gupta, P. K., "Methods in environmental analysis", Water, Soil and Air, Agrobios. India, 2007.

[31] Annual Book of ASTM Standards, Section Eleven, Water and Environmental Technology, 11.01,Water (I-II), 2009.

FREQUENCY CONTROL IN CIGRE LOW VOLTAGE DISTRIBUTION NETWORK WITH SIGNIFICANT AMOUNTS OF INVERTER BASED GENERATORS

Ghullam Mustafa Bhutto*, Muhammad Usman Keerio*, Rameez Akbar Talani*, Ehsan Ali Buriro**

ABSTRACT

Maintaining demand side supply and regulating frequency in power networks are the prime requirements of the modern power systems. The frequency of the power system deviates from its nominal value if there is mismatch between power generation and the consumption. If the active power demand is higher than the active power production in the network, the frequency decreases and vice versa. The increase or the decrease in the frequency can be compensated by balancing the generation and load demands. This is normally done by allocating reserve units or by using inverter based generators such as Battery Energy Storage Devices (BESDs). The main focus of this paper is to control the frequency of the network by providing/absorbing the required/extra amounts of the power by BESDs. The work is done on a simple network and simulations are carried out by using DIgSILENT power factory software version 15.0. The procedure of modeling BES which should operate as Battery Energy Storage equipped Static Compensator (BES-STATCOM) developed in DIgSILENT power factory is also described in this paper.

Keywords: Battery Energy Storage Devices (BESDs), Frequency control, Battery Energy Storage equipped Static Compensator (BES-STATCOM, CIGRE network

1. INTRODUCTION

It is the prime requirement in power systems that the Load-generation must be corrected within short duration; otherwise it might leads to the power line frequency to deviate from the rated value (e.g., 50 Hz in this study). Large deviations in the frequency of the power network cause the threats to the stability and the security of power systems and might cause permanent damage to the equipments [1], [2]. Due to this reason balancing between generation and load in order to regulate the frequency at the nominal value

has gained a vital importance. Several control approaches have been reported in the literature to serve the goal. Some of the power system uses Automatic Generation Control (AGC) technique which issues signals in order to control the reserve units and minimize Area Control Error (ACE), which includes both frequency deviation and unscheduled tie-line power flows [3], [4]. The spinning reserve is also used in order to regulate the frequency. The generators which are used as spinning reserve units automatically increase their outputs when supply is suddenly lost [3]. Furthermore, many generators are equipped with speed governors which adjust their speed depending on the frequency response of the network [5], [6]. The other techniques which are used for this purpose use exciters and Power system stabilizers (PSS) [7]. The problem in such kind of techniques is the time for the switching of the units from off-mode to on-mode. The ESDs are becoming popular for the load-generation balancing in the networks due to their faster response because of the power electronics interfaces as compared to the conventional reserve units such as synchronous generator based reserves. The ESD can store surplus

power produced in the grid and can release the energy into the electricity grid in the case of generation deficit. This property of ES systems can smoothen the short term as well as long-term variations in the power caused by the load variations and behaves like power system balancing and reserve units. The main idea of the study proposed here is about the frequency stability in the CIGRE low voltage distribution network (i.e. developed European CIGRE working group experts) as shown in Fig. 1. This is done by matching load-generation balance in the network shown in Fig. 1. The entire study about the frequency stability within the CIGRE network is not performed here but the CIGRE network shown in Fig. 1 is split into a very simple network comprising finite grid (i.e. a synchronous generator with the active power capability of 30 kW), one battery unit and a load. This is done in order to show the detailed procedure about the control of frequency within the power networks and same procedure is proposed for the frequency stability within the CIGRE low voltage network. The load-generation matching in this paper is done by using 30 kWh BES unit which is modeled as BES-STATCOM for this study. The regulation of the network frequency by using ESDs has already been implemented in several power systems and is available in the literatures.

* Department of Electrical Engineering,

** Department of Electronics Engineering,

Quaid-E-Awam University of Engineering Sciences and Technology, Nawabshah

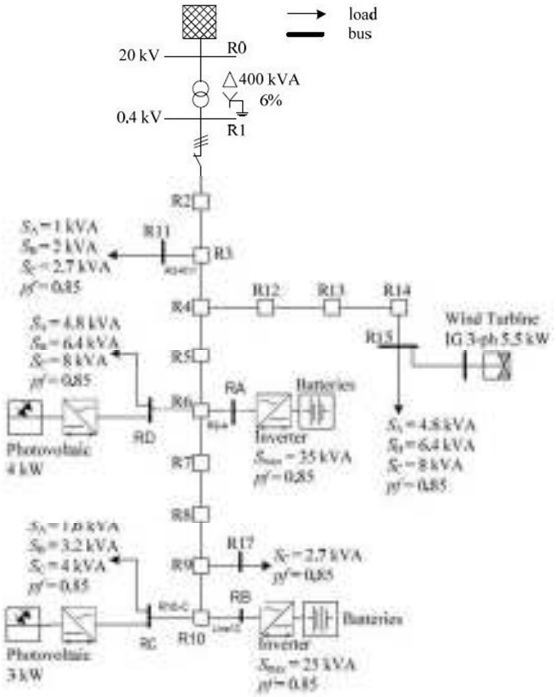

Fig. 2 The single line diagram of CIGRE LV distribution system

The main focus of this paper is to describe the new way of modeling and control set up of the ESD which can operate as BES-STATCOM. The short description about the modeling and the control set up of BES-STATCOM is presented by the author in [8]; this paper gives the detailed description about the development of control system. The developed control system is validated by showing simulation results in this paper. The simple network which comprises a constant impedance load of 30 kW, a synchronous generator which has a capability of providing 30 kW active power and BES unit of 30 kWh energy capacities is used for this study. The modeling and control set up is done in DIgSILENT. The block diagram of the network under the research study in this paper modeled in DIgSILENT is shown in Fig. 2.

It can be seen in Fig. 2 that a battery operating as ESD is connected at DC bus bar of 0.71 kV. The power output of ESD is DC; therefore, a PWM converter is used to transform power into AC from the DC. The DC terminal of the converter is connected at DC bus bar whereas its AC terminal is connected at AC bus bar of 0.4 kV through a series reactor as shown in Fig. 2. A series reactor is used to add some reactance in the network for this study. A synchronous generator of 30 kW operating at unity power factor and a balanced load of 30 kW are also connected at the AC bus bar as shown in Fig. 2.

This paper is organized as follows: Section 2 gives the detailed description about the modeling and the development of the control set up for BES-STATCOM in DIgSILENT power factory software. Section 3 presents the simulation results in order to validate the developed controller. Finally, the conclusion of the paper is presented in section 4.

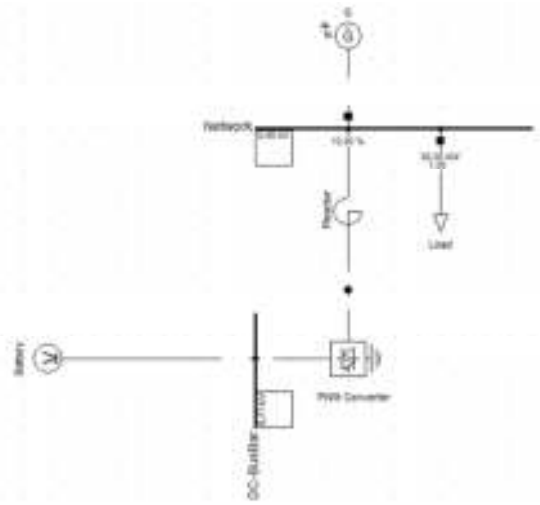

Fig. 3 The block diagram of the network modeled in DIgSILENT

2. METHODOLOGY AND THE DEVELOPMENT OF THE CONTROL SYSTEM FOR ESD

Most of the methods used for battery modeling are complex and time consuming [9-13]. The need for an accurate and complete battery model is dependent on the field of its application. A wide range of battery models are used for simulation studies in various literatures like mathematical, electrical or electrochemical models [14]. The BES-STATCOM in this paper is modeled using a thevenin equivalent representation of the Lithium ion battery and is shown in Fig. 3 [15], [16].

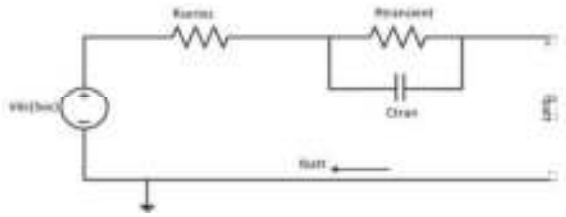

Fig. 4 Electrical model of the Lithium ion battery [15], [16]

This model consists of an ideal voltage source in series with an internal resistance and a parallel RC network. The specifications of a single cell of lithium ion battery are shown in table 1 and are taken from [17]. The built-in model of an infinite DC voltage source is used for the modeling of the BESS in DIgSILENT software [18].

In order to obtain desired amount of power output from the ESD, 170 cells have been connected in series and 6 cells in parallel. The total capacity of ESD in this paper is 42 Ah (i.e. 7 Ah* number of parallel connected cells).

The maximum and minimum voltage of the battery is 714 V (i.e. 4.2* number of series connected cells) and 425 V (i.e. 2.5* number of series connected cells) respectively. As the power output of the battery is DC, an inverter is used to convert DC power into AC power. The PWM inverter is modeled in DIgSILENT according to the reference [19].

Table 1 Battery Specifications for a single cell

Parameter	Value
Capacity	7 Ah
Nominal Voltage	3.7 V
Maximum Voltage	4.2 V
Minimum Voltage	2.5

In order to obtain RMS simulation results and controlling the charge/discharge rate of the ESD, it is necessary to develop the DIgSILENT Simulation Language (DSL) model of the battery and its controller. The composite model made in DIgSILENT, showing signals coming in out of respective blocks is shown in Fig. 4.

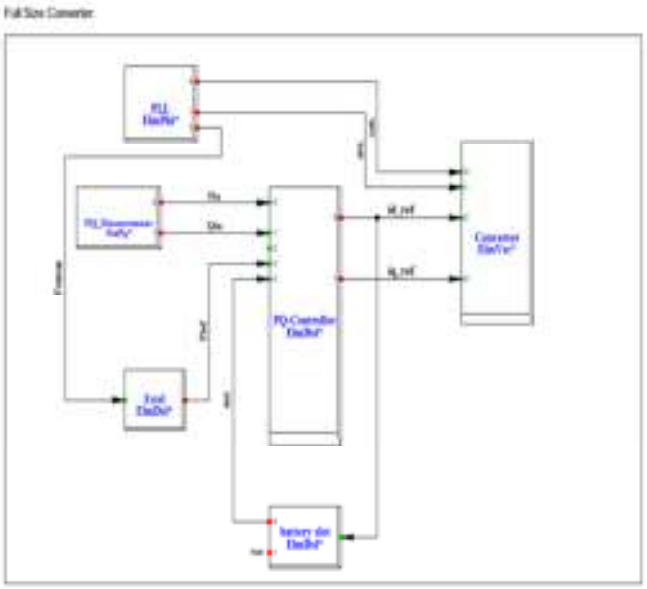

Fig. 5 The composite frame model of BES-STATCOM

There are different blocks used in this model, some of them are measuring bocks and others are DSL models. The blocks showing "Sta, ElmPhi, and ElmVsc" representations are the measuring blocks and the blocks showing "ElmDsl" require DSL modeling. The PLL block is used to measure the angle and the frequency of grid voltage and send the respective signal to the converter and the frequency controller. The DSL model of the frequency controller is shown in Fig. 5. This controller compares measured and reference frequency and sends the error signal to PI controller to generate Pref.

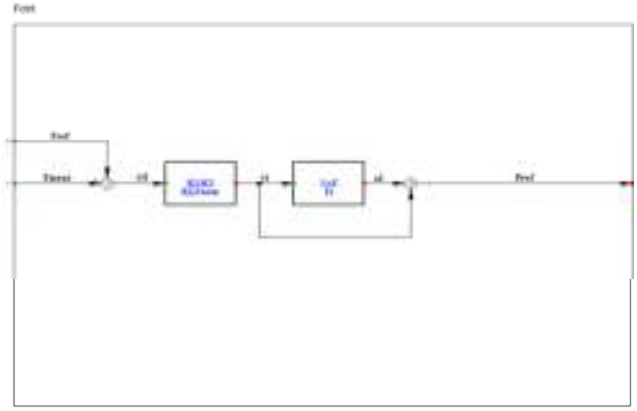

Fig. 6 The DSL model of frequency controller

The block representing PQ measurement shown in Fig. 4 is used to measure active and reactive power at the AC bus. The active and reactive power 'Pin' and 'Qin', the active power reference 'Pref' sent by the frequency controller and battery State Of Charge 'SOC' are the inputs to the PQ controller slot as seen in Fig. 4. Its outputs are active current reference (idref) and reactive (iqref) currents references. These currents references will be sent to current controller which will decides the duty cycle for the switches used in the converter [20]. The DSL model of PQ controller is shown in Fig. 6. The active current reference (idref) is sent to the battery slot (see Fig. 4) where it will be integrated in order to get the charge. Due to safety concerns the battery SOC is limited within 20-95% in order to avoid damage of the battery and to preserve battery life, [16]. The details about the DSL modeling of battery slot and the explanations about the DSL model of PQ controller shown in Fig. 6 are presented in [8].

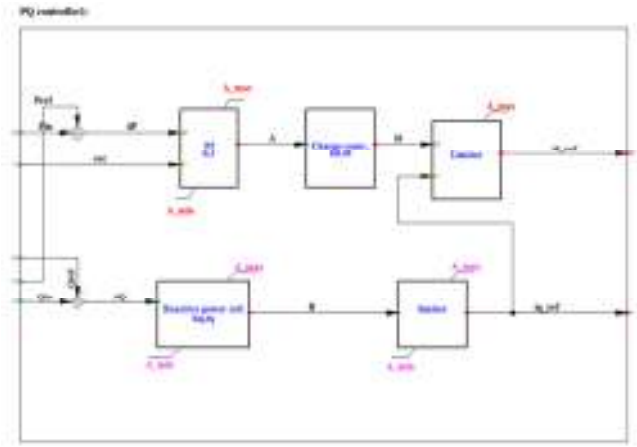

Fig. 7 The DSL model of PQ controller

3. SIMULATION RESULTS

In the normal operation, the load active and reactive power requirements are delivered by a synchronous generator. Active power injection by the BES-STATCOM is zero in this condition and the power system operates at

its nominal frequency and voltage limits. Since synchronous generator can only provide 30 kW, if the load is increased more than this limit then there will be problem with the network frequency unless it is supplied by the battery. To analyze the power system frequency response of the distribution network shown in fig. 2, a step increase/decrease in the active power of a system load is simulated here. When the demand is increased, the system frequency decreases. A step load increase of 90% is applied at the time equal to t=40 sec on the system load. The load with step applied becomes 57 kW in this condition. The synchronous generator is delivering 30 kW and remaining 27 kW power is supplied by the battery. The PI controller of the active power control loop shown in fig. 5 generates a current reference at 40 sec in this condition. When the battery is discharged down to 20%, the current output of this PI controller reaches to zero. The output of the PI controller is sent to the charge controller which controls the charge/discharge rate of the battery. The study of the same battery which is used in CIGRE low voltage distribution network in the case of different charging rates is given in [8], [21]. The battery is delivering current to the load at full charging rate (i.e. 1 C rate) in this condition. The current delivered by the battery in this case is shown in Fig. 7.

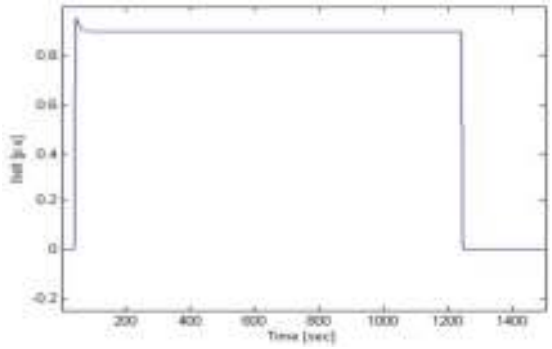

Fig. 8 Battery current at full charging rate

This current as shown in Fig. 7 is sent to the battery slot where it is integrated to obtain the charge.

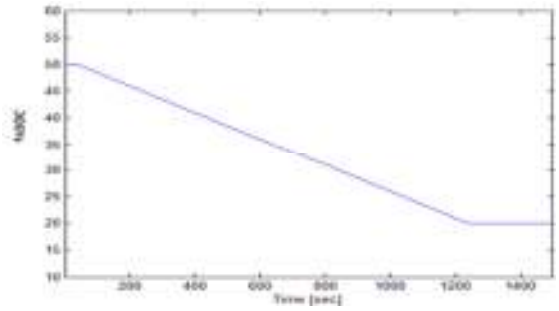

Fig. 9 percent SOC of battery

The discharge capacity of the battery depends on how fast battery is discharging. Higher the discharging rate, lower the time required for the battery to be discharged and vice versa [22], [23]. The SOC of battery with the above load step is shown in Fig. 8.

The battery charge/discharge rate is defined in the PQ controller shown in Fig. 6. Discharging of battery starts at 50% because this limit has been set as an initial condition for charge/discharge in the DSL model of the battery [8], [21]. The frequency of the network with the above load step applied is shown in Fig. 9.

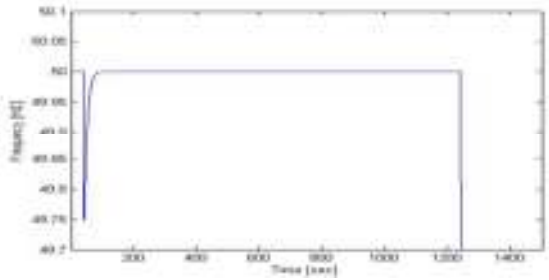

Fig. 10 Frequency of the network

As seen in Fig. 9 that frequency decreases at 40 sec due the increased load demand and is controlled by the ESD in a short period by injecting desired amount of the power. When battery is discharged down to the limit of 20%, it has no more power to supply the load. The frequency in this case when battery has been fully discharged reduces drastically and the system enters into unstable condition as shown in Fig. 9.

Again a load step of -90% is applied at time, t=40 sec on the system load. The load demand with this step applied decreases and becomes 3 kW. The synchronous generator of 30 kW is delivering 3 kW to the load and remaining 27 kW power of the generator is used to charge the battery. The PI controller responsible for active power loop of PQ controller shown in Fig. 6 generates a current reference at 40 sec in this condition.

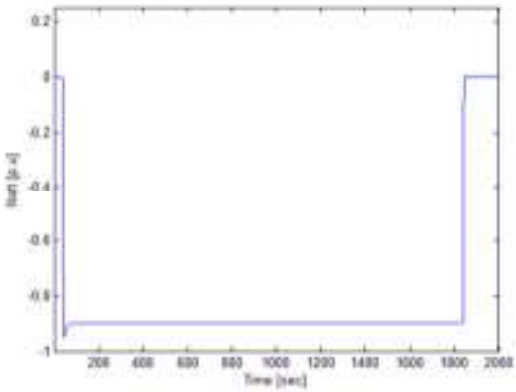

Fig. 11 The current flowing to charge battery units at full charging rate

When the battery is charged up to 95%, the current output of this PI controller reaches to zero. The output of the PI controller is sent to the charge controller which controls the battery charging rate. The battery charges at full

charging rate (i.e. 1 C rate) in this condition. The current going into the battery in order to charge it in this case is shown in Fig. 10.

The battery SOC and the network frequency are shown in Fig. 11 and Fig. 12 respectively. As seen in Fig. 11 the battery is charged up to 95% in half hour (i.e. 1800 sec) because initial SOC of a battery is at 50% in the beginning of simulation results.

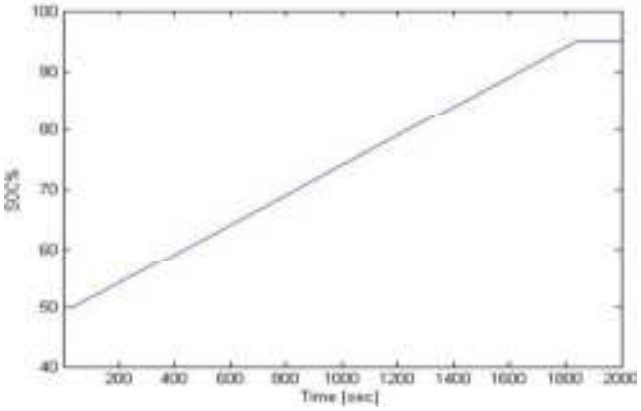

Fig. 12 Percent SOC of ESD

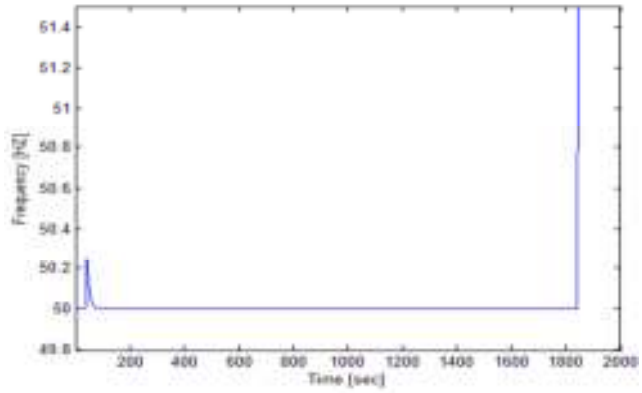

Fig. 13 Frequency of the network

It can be seen in Fig. 12 that frequency of the network increases at 40 sec due the decreased load demand and is controlled by the battery in a short period by absorbing extra amount of the power supplied by the synchronous generator. When battery is charged up to the limit of 95%, it cannot absorb more power; therefore, frequency of the network is increasing very fast and the system enters into unstable condition.

4. CONCLUSIONS

The study about the constancy of the frequency of power system has been carried out in this paper. The study is performed on a very simple network and these concepts are proposed for the frequency stability within the CIGRE low voltage distribution networks and other networks like that. The development of BES-STATCOM controller for ESDs has been described here and the developed controller has been validated by using simulation results. Different scenarios such as load reduction or generation deficit have been studied in this paper. It has been proved with the help of the simulation results that the ESDs in all the conditions have successfully restored the frequency of the network within a short duration. The study about the islanding, voltage and the frequency control in islanded portion of the CIGRE low voltage distribution network will be done in the future.

References

[1] P. M. Anderson and M. Mirheydar, “An adaptive method for setting under frequency load shedding relays”, IEEE Trans. on Power Systems, vol. 7, no. 2, pp. 647-655, 1992.

[2] A. Molina-Garcia, F. Bouffard and D. S. Kirschen, “Decentralized demand-side contribution to primary frequency control” IEEE Trans. on Power Systems, vol. 26, no. 1, pp. 411-419, 2001.

[3] D. S. Callaway and I. A. Hiskens, “Achieving controllability of electric loads”, Proc. of the IEEE, vol. 99, no. 1, pp. 184-199, 2011.

[4] M. Ilic and Q. Liu, “Toward sensing, communications and control architectures for frequency regulation in systems with highly variable resources”, Control and Optimization Theory for Electric Smart Grids, New York: Springer, 2011.

[5] D. Trudnowski, M. Donnelly and E. Lightner, “Power system frequency and stability control using decentralized intelligent loads”, in Proc. Of the 2005 IEEE Trans., Dallas, TX, May 2006.

[6] J. Dong, J. Zuo, L. Wang, K. S. Kook, I. Chung, Y. Liu, et al., “Analysis of power system disturbance based on wide-area frequency measurements”, in Proc. of the IEEE Power and Energy Society General Meeting, Tampa, FL, Jun. 2007.

[7] P. Kundur, Power System Stability and Control, New York: McGraw Hill, Inc., 1994.

[8] Ghullam Mustafa, B. Bak-Jensen, P. Mahat, “Modeling of the CIGRE Low Voltage Test Distribution Network and the Development of Appropriate Controllers”, International Journal of Smart Grids and Clean Energy (SGCE), Vol. 2 No. 2, pp. 184-192, 2013.

[9] D. W. Dennis, V. S. Battaglia, and A. Belanger, “Electrochemical modeling of lithium polymer batteries”, J. Power Sources, vol. 110, no. 2, pp. 310-320, 2002.

[10] P. M. Gomadam, J.W. Weidner, R. A. Dougal, and R. E. White, “Mathematical modeling of lithium-ion and nickel battery systems”, Journal of Power Sources, vol. 110, no. 2, pp. 267-284, Aug. 2002.

[11] R. C. Kroeze and P. T. Krein, "Electrical battery model for use in dynamic electric vehicle simulations", Proc. of IEEE Power Electronics Specialists Conference, Rhodes, Greece, pp. 1336-1342, June 2008.

[12] Z. M. Salameh, M.A. Casacca, and W.A. Lynch, "A mathematical model for lead-acid batteries", IEEE Trans. on Energy Conversion, vol. 7, no. 1, pp. 93 – 98, Mar. 1992.

[13] K. Yoon-Ho and H. Hoi-Doo, "Design of interface circuits with electrical battery models", IEEE Trans. On Industrial Electronics, vol. 44, no.1, pp. 81 – 86, Feb. 1997.

[14] D. Linden, "Handbook of Batteries and Fuel Cells", McGraw-Hill, New York, 1984.

[15] Tremblay, O. Dessaint, L.-A. Dekkiche, A.-I, "A Generic Battery Model for the Dynamic Simulation of Hybrid Electric Vehicles", Vehicle Power and Propulsion Conference, VPPC, pp. 284-289, 2007.

[16] Low Wen Yao, Aziz, J.A, "Modeling of Lithium Ion Battery with Nonlinear Transfer Resistance", IEEE applied power electronics Colloquium (IAPEC); 2011.

[17] Data sheet of Rechargeable Lithium-ion battery Li Ion Saft VL37570:pdf available on www.saftbatteries.com.

[18] Technical reference for DC voltage source in DIgSILENT.

[19] Technical reference for PWM inverter published by DIgSILENT GmbH,, Germany.

[20] J. Svensson, "Grid-connected voltage source converter, control principle and wind energy applications", PhD dissertation, Chalmers University of Technology, Gothenburg, Sweden, March1998.

[21] Ghullam Mustafa, B. Bak-Jensen, P. Mahat, and P.F. Ribeiro, "Mitigation of voltage sags in CIGRE Low Voltage Distribution Network", Proc. of the 5th IEEE PES Asia-Pacific Power and Energy Engineering Conference, APPEEC 2013, IEEE Press, 2013.

[22] Lithium-Ion Batteries: Individual Data Sheet CGR18650, 2000. Panasonic.[Online]. Available: http://www.panasonic.com/industrial/ battery.

[23] Hard Carbon Lithium Ion Rechargeable Battery, 2001.Sony.[Online]. Available: http://www.sony.co.jp/en/Products/BAT/ION/Cataloge. pdf

PASSIVE CONTROL OF MIXING BY FLOW PULSATION IN A CURVED PIPE

Fareed Hussain Mangi*, Kashif Hussain Mangi**, Saleem Raza Samo*,
Abdul Rehman Jatoi*, Zafar Ali Siyal*

ABSTRACT

Mixing enhancement usually referred to the reduction of non-homogeneities. Mixing operations are encountered widely throughout industrial processes in different energy systems and chemical reactors involving physical and chemical change. The requirement of this process has always been to obtain an energy efficient and environmental friendly mixing in multifunctional heat exchangers/chemical reactors. Poor mixing can affect the product quantity and quality as well as other losses.

The passive control of mixing enhancement is meant to the special surface geometries or fluid additives. This work emphasizes on the tracer deformation and analysis of cross-sectional concentration distribution due to imposition of pulsation. An experimental system comprising of a pulsation generator (scotch-yoke mechanism), a 90° curved pipe and a tracer injection system is used. Measurements are carried out by a Planar Laser-Induced Fluorescence (PLIF) technique. To avoid laser light diffraction effects during experiments, a T-shaped flow divider are installed at the exit of the 90°curved pipe. The measurements are carried out for a range of steady Reynolds number Re_{st} [420-1000] and different values of Womersley frequency parameter α for a velocity amplitude ratio β = 1. Tracer distribution due to pulsation in a curved pipe flow is observed. Effects of pulsation on the mixing in laminar flow regime are analyzed. The results showed an important and encouraging role of pulsatile flow on mixing enhancement.

Keywords: *Chaotic advection - Pulsatile Flow - Mixing enhancement - PLIF measurements.*

1. INTRODUCTION

Mixing operations are encountered widely throughout industrious processes involving physical and chemical change. Therefore mixing is an essential feature of many processes in food, pharmaceutical, paper, plastics, ceramics and rubber industries. Mixing in the laminar flow regime occurs in many industrial processes especially in chemical and pharmaceutical ones.

In order to enhance mixing, different geometries more or less complex have been studied, i.e. closed configurations where fluid flow is confined in a volume [1] and open ones [2] and [3]. Previous studies of [1], [4] and [5] show that geometrical modifications to a steady curved pipe flow have an important influence on mixing and heat transfer.

Furthermore, by imposing pulsation to convert the steady flow into a pulsatile flow; some important alterations in the secondary flow in terms of stretching and folding of Dean Roll cells have been observed. Therefore, controlling pulsation parameters, one can make this flow much more complex and favorable for efficient mixing. Pulsatile flow is a periodical oscillating flow superimposed on a steady flow in the laminar, transitional and turbulent flow regimes. Pulsatile flow has many applications in industrial and medical applications, including heat transfer intensification, fluid mixing enhancement, augmentation of cleaning, mass transport in porous media, thermo acoustic devices, reciprocating and micro pumps, and bio fluids engineering, etc. The Pulsatile flow in a curved pipe has been the focus of research since many years. The main focus of most of the previous studies in this domain was on physiological flow applications [6], [7], [8], [9]. Pulsatile flow in a curved pipe as an application of heat transfer enhancement in industrial energy systems has also been studied by [10], [11], [12], [13], [14], [15] and [16].

This work contributes to the estimation of mixing enhancement by flow manipulation in a curved pipe. Planar laser induced fluorescence technique (PLIF) is used to highlight the information of a tracer distribution by using the pulsation conditions for a range of steady Reynolds number [420-1000] and different Womersley frequency parameter α and velocity amplitude ratio β=1. Tracer deformation due to pulsation in a curved pipe flow is observed. Effects of different pulsation parameters on the mixing in laminar flow regime are analyzed.

* Energy and Environment Engineering Department, Quaid-e-Awam University of Engineering, Science and Technology Nawabshah

** Chemical Engineering Department, University of Karachi

This paper is organized as follows: in the Section 2 materials and methods are described, Section 3 is devoted to the explanation of the experimental setup, Section 4 is expresses the measurements and the PLIF calibration, Section 5 is discussing the results and in Section 6 the works are concluded.

2. MATERIALS AND METHODS

2.1 Pulsatile Flow

The pulsatile flow used in this study is a result of a pure sinusoidal flow imposed on a steady flow. Therefore analyzing pulsatile flow, it is obvious to consider the fluid motion as composed of a steady flow and a pure sinusoidal term. The equation (1) for the pulsatile velocity U_P can be written as:

$$U_P(t) = U_{st} + U_{sin}(t) \quad (1)$$

where U_{st} is the mean steady velocity and $U_{sin}(t)$ is the pure sinusoidal flow, which is the time-dependent component of the pulsatile velocity. If the amplitude of the sinusoidal flow is $U_{sin\,max}$, and the angular frequency of the oscillation is ω, then Eq. 1 can be written as:

$$U_P(t) = U_{st} + U_{sin\,max}\ \sin(\omega t) \quad (2)$$

The angular frequency, ω , can also be described by a dimensionless parameter, α , called the Womersley parameter, defined as:

$$\alpha = r_o\left(\frac{\omega}{\vartheta}\right)^{\frac{1}{2}} \quad (3)$$

where r_o is the radius of the pipe and ϑis the kinematic viscosity of the fluid. The Womersley number is a dimensionless expression of the inertial effects due to pulsatile flow frequency in relation to viscous effects and is used in what follows to express the angular frequency of the oscillation.

A velocity amplitude ratio β is defined as the ratio between the maximum sinusoidal amplitude of the sinusoidal velocity term and the average value of the steady velocity term. Mathematically:

$$\beta = \frac{U_{sin\,max}}{U_{st}} \quad (4)$$

2.2 Mixing Quantitative description of mixing

Quality or goodness of mixing of a given mixture can be developed by the comparison of the state of the mixture to the most complete mixing state achievable. The complete mixing corresponds to the statistical randomness of the ultimate properties of the ingredients being mixed which would follow the binomial distribution. Different parameters of mixing quantification are discussed as follows.

Mean concentration

If one makes N measurements of concentration, of C_i of one of the components, then the mean concentration $\bar{C}$ is calculated according to

$$\bar{C} = \frac{1}{N}\sum_{i=1}^{N} C_i \quad (5)$$

where $\bar{C}$ should not differ significantly from the overall concentration of the component, the difference between $\bar{C}$ and overall concentration of the component decreases as the number of characterized samples N is increased. The measured concentration values of the minor component also depend on the sample size. These values approach the overall concentration of the minor component as the sample size is increased.

Variance

A basic measure of homogeneity of a mixture is the extent to which the concentration values at various regions of the volume of the mixture differ from the mean concentration. The variance σ^2 arising from the individual concentration C_i measurements provides such an index to quantitatively assess the degree of mixing. The variance σ^2 is expressed as

$$\sigma^2 = \frac{1}{N}\sum_{i=1}^{N}(C_i - \bar{C})^2 \quad (6)$$

A small variance implies that most of the samples yield concentration C_i values are close to the mean $\bar{C}$ of all samples, thus suggesting a homogeneous system.

Standard deviation

The deviation of the sample measurements from the mean $\bar{C}$ is given by the standard deviation:

$$\sigma = \sqrt{\sigma^2} \quad (7)$$

This is the square root of the variance, and is in the same unit as the concentration data.

Coefficient of variation C_oV

When the means of two concentration data sets differ greatly, a measure of relative variability is defined with coefficient of variationC_oV.

$$C_oV = \frac{\sigma}{\bar{C}} \quad (8)$$

Maximum variance

$$\sigma^2_{max} = \bar{C}(1 - \bar{C}) \quad (9)$$

The maximum variance occurs if the components are completely segregated.

Intensity of mixing

One can define intensity of mixing I_{mix} as:

$$I_{mix} = 1 - \frac{\sigma^2}{\sigma^2_{max}} \quad (10)$$

Intensity of mixing values range from zero, for completely segregated to one for ideally homogeneous system.

3. EXPERIMENTAL SETUP

Fig. 1 illustrates the experimental setup used in this work. The circular water duct made up of Plexiglas was used to provide controlled flow through the test section. Steady flow is pumped in the setup through a volumetric pump from a tank of 300 L capacity. The steady flow rate is measured by an electromagnetic flow meter. Pulsations are superimposed on the steady flow by a scotch yoke pulsation generator. To be sure about clean and stable inlet conditions and to develop a Poiseuille flow in the setup a straight 2.50 m pipe is used. The scotch yoke pulsation generator allows adjusting different pulsation conditions by regulating the dimensionless frequency parameter α and amplitude ratio β. This scotch yoke mechanism consist a crank of 40 mm diameter connected by a metallic stem. The piston stroke is controlled on the crank in steps of 20 mm to a maximum of 200 mm. A motor speed reducer is used to control the pulsation frequencyω.

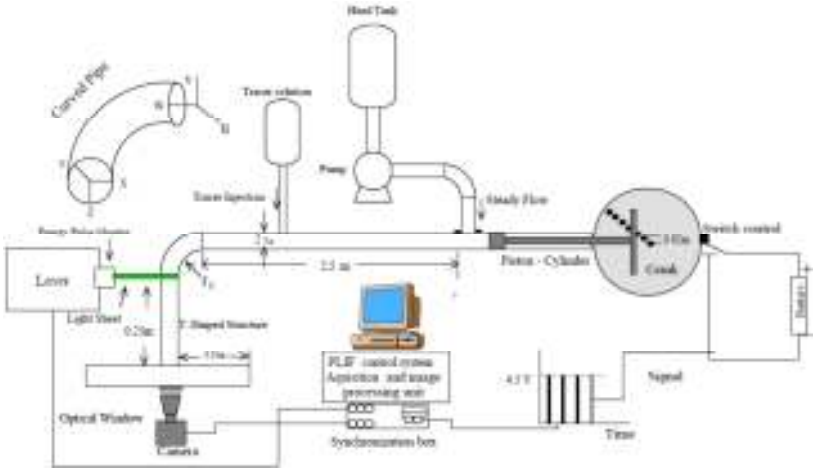

Fig. 1. Experimental setup.

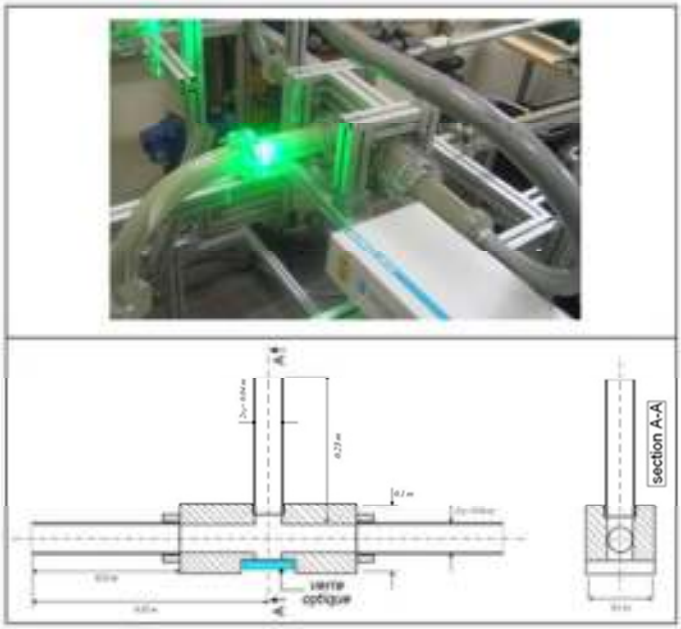

Fig. 2. T-shaped flow divider.

Therefore both parts of the flow i.e. steady and sinusoidal join upstream of the curved pipe in such a way that a fully developed flow enters in the 90° curved pipe of 40 mm diameter, radius of curvature 220 mm. A tracer injection setup was designed and fabricated to inject the tracer dye through an injecting needle of 1 mm diameter. Injecting needle was positioned at the center of the cross-sectional area of the duct.

A T-shaped Plexiglas flow separator shown in Figure 2, comprising a central tube with two symmetric pipe sections of the equal diameter as the 90° curved pipe (40 mm) is installed at the exit of the curved pipe to avoid the light refraction effects during PLIF measurements. The middle straight pipe section connected to the 90° curved pipe outlet is passed through a water box to get better flattened image quality.

3.1 PLIF Measurements

The Planar Laser Induced Fluorescence (PLIF) technique is an optical method to obtain instantaneous concentration (or temperature) measurements: it is used to determine the concentration spreading in the secondary flow at the exit of the curved pipe. A Nd YAG laser (50 mJ, 532 nm) with sheet thickness 2 mm and a recording camera (7 Hz) are used. The camera is equipped with a lens (focal distance of 60 mm) and is placed with a filter in front of the optical window; the laser sheet illuminates the outlet of the curved pipe (Fig. 1). The injected tracer dye is Rhodamine B. The resolution of each picture is 2048×2048 pixels. A Dantec Dynamics processing system is used to obtain the concentration distribution information. Except in the steady-state flow cases, the measurements for pulsatile flows are time-dependent and need a synchronization system. Thus the acquisition system is connected to an electric power source controlled by a switching contact device. Each contact of the switch and the small knob fixed on the periphery of the crank sends a 4.5 V signal to the acquisition system. The acquisition occurs after a delay that can be calculated based on the desired phase position and the angular velocity of the crank. The measurements are obtained in the four principal phase positions: $\omega t = 0°, 90°, 180°$ and $360°$.

4. MEASUREMENTS AND CALIBRATION

The different conditions of pulsation cases are obtained with the adjusting the different parameters shown in the Table 1.

Table 1. The different conditions of pulsation.

Re_{st}	U_{st} (m/s)	β	α
420	0.0105	1	10
600	0.015	1	10
800	0.020	1	10
1000	0.025	1	10

4.1 PLIF Calibration

Planar Laser-Induced Fluorescence is an optical-based technique used to perform nonintrusive whole field concentration measurements in liquids. There exists a well-defined relationship between the intensity of fluorescence and concentration when all other experimental parameters are fixed, which allows deriving a calibration curve for the intended measurement.

The fluorescent dye used in the present study is Rhodamine 6G with calibration range between zeros to a maximum concentration of 100 micrograms per liter. The camera filter is replaced by a 570 nm cut-off filter to ensure the fluorescent light to be captured while adequately suppressing the 532 nm laser light. To get reference PLIF images, a series of images of a calibration test section corresponding to different concentrations is recorded. A series of 50 images for each concentration ranging between 0 to 100 µg/L of a calibration test section corresponding to different concentrations is recorded. The gray value response of the camera is then monitored to ensure a linear response to the dye concentration. This procedure is used to find the appropriate maximum concentration solution. Calibration curve is obtained in such a way that the experimental setup, laser and the optical arrangements are on the same positions. An analog beam monitor is also used to monitor the laser energy. To calibrate a LIF setup, images must first be acquired at known experimental conditions i.e. concentration or intensity of laser and stored as calibration images. For this calibration the intensity of laser light for all concentrations are constant.

In the Fig. 3, the linearity between the fluorescence signal (grey-level) and concentration defined locally is observed. Camera is sensible to detect even small concentration of 1.50 µg/L. Fig. **3**. Calibration curve. The calibration curve includes for each and every pixel in the entire image, some of these will have stronger response to varying concentrations, and some will have weaker response.

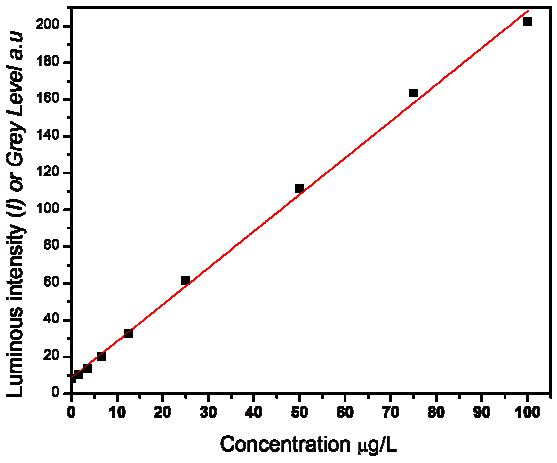

Fig. 3. Calibration curve.

The vertical bars illustrate the level of variation in Luminous intensity/gray scale values when nominal concentration and laser energy is otherwise constant. The units of the luminous intensity are a.u. (arbitrary units). The measurements are carried out with an intensive surety of keeping the experimental conditions right from the calibration to the final experimental measurements constant. This means the laser intensity, camera aperture and position remain unchanged. The concentration C is then assigned to the detected fluorescence intensity I for each pixel P(i,j) of the CCD camera (i = 1...2048, j = 1...2048). A linear correlation between I and C is verified. The calibration curve starts from a level different to zero, due to the luminosity in the laboratory. It can be observed that the camera used is sensible to detect even small concentration of 1.50 µg/L. The error in amount of colorant injected and amount of colorant measured/captured by the camera was found from 9% to maximum 15 %.

5. RESULTS AND DISCUSSIONS

5.1. Qualitative Measurements

A comparison of the results of a tracer deformation in steady and pulsatile flow cases shows the influence of the pulsation on the mixing in a 90° curved pipe. Rhodamine 6G as a tracer was injected through an injection system by a needle of 1 mm in diameter. The tracer injection position was at the center of the pipe section.

For the steady Reynolds number $420 \leq Re_{st} \leq 1000$, tracer mark was always with a constant mark in the upper part of the pipe section. This was moving slightly back to the left side of the upper side pipe section with the increase in steady Reynolds number.

When the velocity amplitude ratio is unity ($\beta = 1$) the tracer is deformed in the boundary layer near the wall in the upper part of the section.

5.1.1. Flow visualization for Steady Cases

In the steady flow, the tracer injected in at the center of the pipe follow the streamlines of the main flow and remains near the upper wall by occupying a constant and very small space. But on the other hand when looking at qualitative images, the tracer dye deforms well and occupies the more space in pipe with the pulsation impositions on the steady flow. This is may be due to the disturbing Dean Roll cells structures by pulsations. Qualitative images show that tracer distribution for steady Reynolds numbers Re_{st} lies in the upper part at the exit of a 90° curved pipe. When the velocity amplitude ratio β is unity with a constant frequency parameter α, tracer distribution is increasing in the cross-sectional area. More homogeneity is visualized by increasing steady Reynolds number Re_{st}. For a constant steady Reynolds number and a constant velocity amplitude β with the variation of frequency parameter α, the secondary flow remains more or less the same in structure.

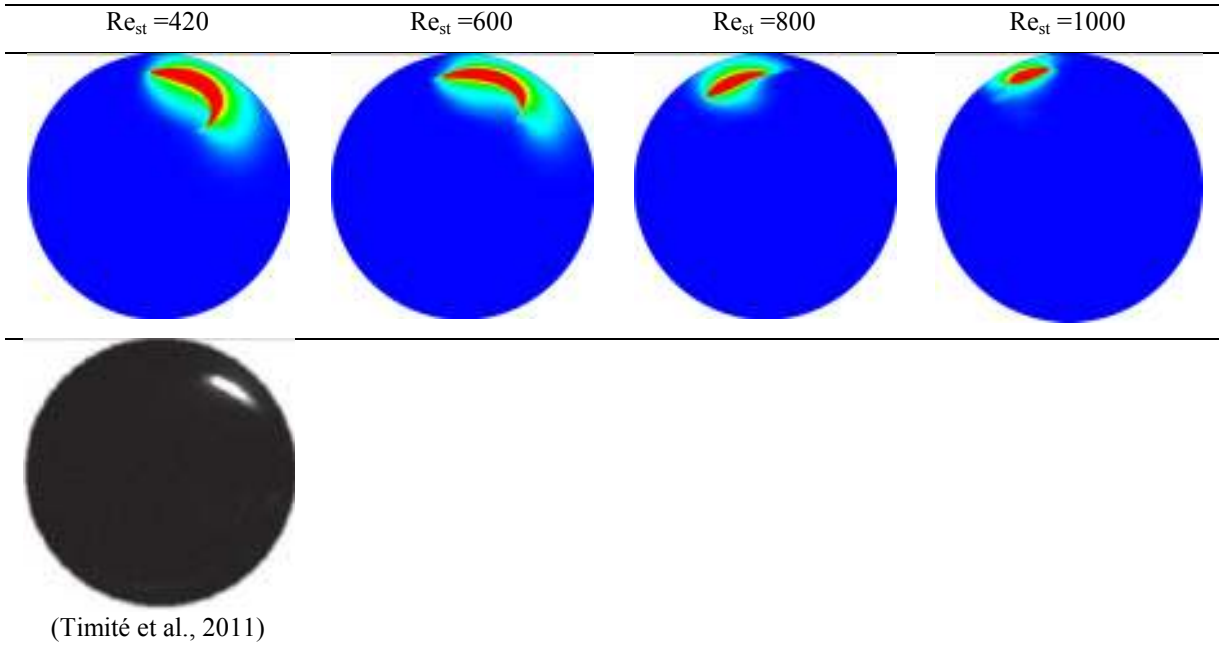

Fig. 4 Qualitative images at the exit of a 90° curved pipe for different Reynolds numbers.

Fig.4 show the chaotic behavior of the fluid particles at the exit of a 90° curved pipe when there is no pulsation imposed. In the steady state flow fluid particles do not diverge and remain always in the upper part of the cross-section with occupying more or less same amount of area. The tracer line decreases with increasing Reynolds number. This is because the rate for colorant injection is constant for all cases. Therefore with the high Reynolds numbers the colorant mixes well and we observe the less tracer line in the cross sectional area.

.

5.1.2. Flow visualization for pulsated case, α=10, β = 1

Fig5 presents the qualitative images of $Re_{st} \leq 1000$, $\alpha = 10$ and $\beta = 1$, the fluid particles deviation is clear in the images and tracer occupy much more surface than the steady state cases. The first qualitative observation for an injection at center of the pipe section proposes that particle trajectories can be spatially chaotic in pulsatile alternating Dean Flow and certain zones in the flow are more likely than others to intensifying this deviation

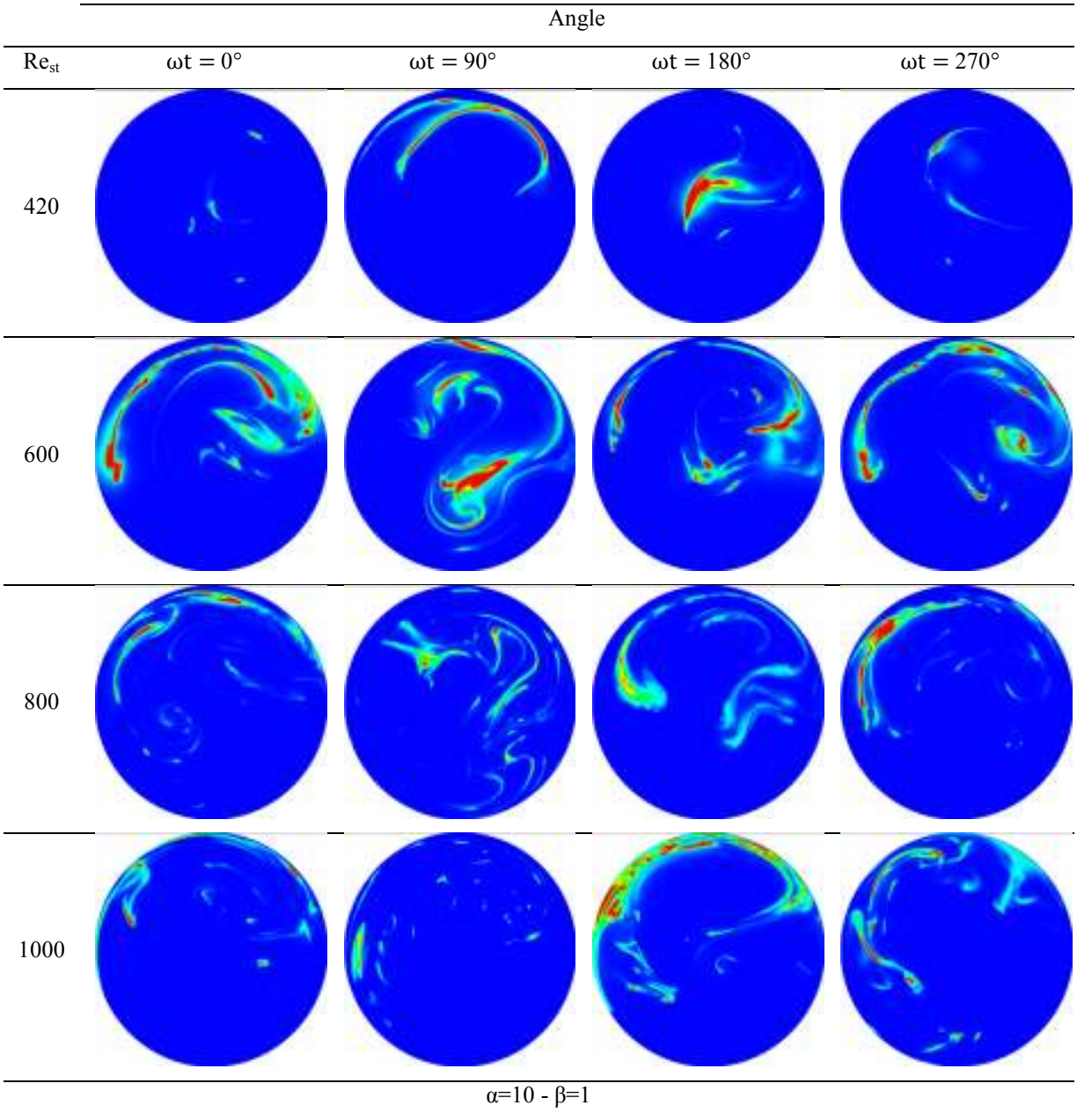

Fig. 5. Qualitative images at the exit of a 90° curved pipe for different Reynolds numbers of same pulsation condition α=10 - β=1.

5.2. Quantitative Measurements

5.2.1 Mixing enhancement during different phase angles.

Figure 6 represents mixing degree versus the phase angle ωt over an oscillation period for Re_{st}=420, 600, 800 and 1000 and α=10 and β=1. Here mixing degree increases between phase angles of 0° and 90° for all cases except in pulsation case of Re_{st} =420 where we observe the maximum Degree of mixing about 0.65 at phase angle ωt=270°.

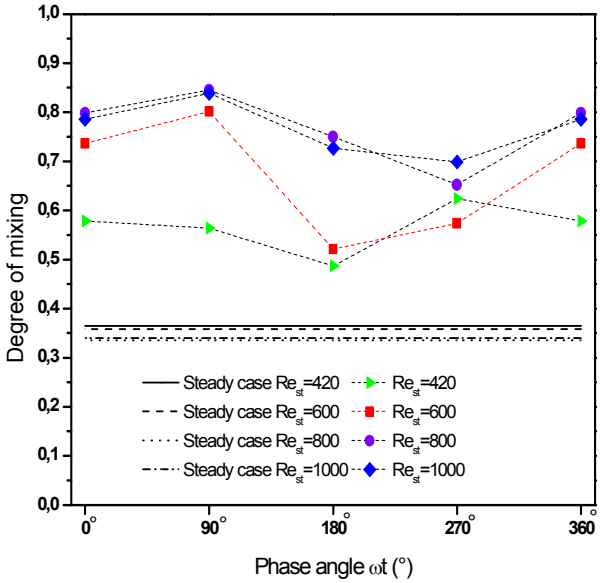

Fig. 6 Influence of phase angle ωt on mixing intensity for α=10 and β=1

The mixing degree increases between phase angles of 0° and 90° for α≤10. Then it gradually decreases in the phase 180° of the oscillation period. Beyond this phase angle, it increases again until the phase 270°. The increasing mixing degree in a phase between 0° and 90° in the oscillation period can be attributed to the acceleration of the flow in this part of the oscillation period (see [14] and [15], the vorticity and the strain rate play a significant role in transverse mixing increase between 0° and 90°).

5.2.2 Mixing Enhancement After a Complete Pulsation Cycle.

Figure 7 shows the influence of Re_{st} on the enhancement of mixing as the function of steady Reynolds number Re_{st} for constant velocity amplitude ratio β=1. The degree of mixing represented in the Figure 7 is calculated at phase angle ωt=360°, it means after a complete pulsation cycle. Degree of mixing increases as Re_{st} increases for pulsated cases. The maximum value of Degree of mixing 0.75 is obtained for Re_{st}= 1000 and α=10.

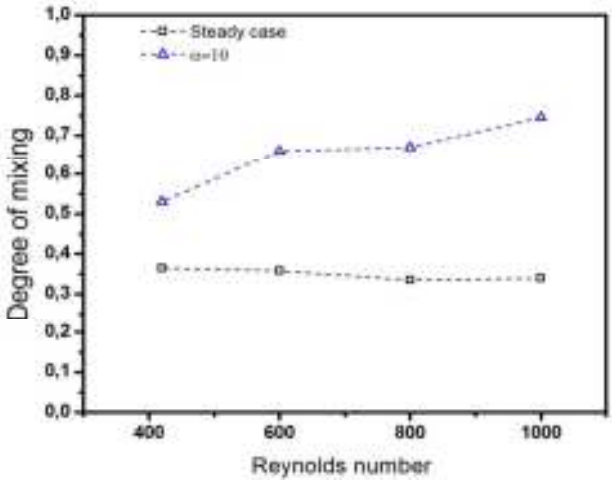

Figure 7 Mixing enhancement after a complete pulsation cycle for α=10 and β=1 at ωt=360°.

6. CONCLUSIONS

Planer Laser Induced Florescence (PLIF) technique is used to study the concentration field in a developing laminar pulsatile flow in a 90° curved pipe. Planar laser induced fluorescence technique is for the first time used in the laboratory. Calibration of the experimental setup with PLIF technique is a delicate process and it takes a lot of time to perform the experiments for the different pulsation conditions. The PLIF measurements are carried out for Reynolds numbers Re_{st}=420, 600, 800 and 1000 both for steady cases and pulsatile flows with Womersley number α=10 and velocity component ratio β=1. The effects of these parameters on the mixing intensification are studied. The PLIF results of secondary flow for four different phase positions ωt=0°, 90°, 180° and 270° are analyzed. The detailed PLIF measurements of the secondary flow showed that pulsatile flow in a curved pipe has a great influence on mixing enhancement. The arrangement of the three control parameters: Reynolds number Re_{st}, frequency parameter α and velocity amplitude ratio β extracts the consequential flow extremely complex.

The influence of Re_{st}, α and β on mixing degree is analyzed. For pulsation cases, degree of mixing increases with the Reynolds number.

In summary, the experimental results showed some information on tracer transportation and diffusion. The first type of information is related to the stretching and folding mechanisms of tracer due to pulsation. Secondly flow visualizations showed that the pulsation works well to amplify the mixing by diffusing the tracer lines in a larger space of the 90° curved circular pipe section.

Analysis of the dye deformation suggested that the pulsation imposition on a flow in 90° bend can generate better mixing.

REFERENCES

[1] AREF, H. 1984. Stirring by chaotic advection. Journal of Fluid Mechanics, 143, 1-21.

[2] JONES, S. W., THOMAS, O. M. & AREF, H. 1989. Chaotic advection by laminar flow in a twisted pipe. Journal of Fluid **Mechanics**, 209, 335-357.

[3] KHAKHAR, D. V., FRANJIONE, J. G. & OTTINO, J. M. 1987. A case study of chaotic mixing in deterministic flows: The partitioned-pipe mixer. Chemical Engineering Science, 42, 2909-2926.

[4] Acharya, N., Sen, M. & Hsueh-Chia, C. 1992. Heat Transfer Enhancement In Coiled Tubes By Chaotic Mixing. International Journal Of Heat And Mass Transfer, 35, 2475-2489.

[5] Mokrani, A., Castelain, C. & Peerhossaini, H. 1997. The Effects Of Chaotic Advection On Heat Transfer. International Journal Of Heat And Mass Transfer, 40, 3089-3104.

[6] Pedley, T. J. 1980. The Fluid Mechanics Of Large Blood Vessels / T. J. Pedley. London : Cambrige University Press.

[7] Chang, L. J. & Tarbell, J. M. 1985. Numerical Simulation Of Fully Developed Sinusoidal And Pulsatile (Physiological) Flow In Curved Tubes. Journal Of Fluid Mechanics, 161, 175-198.

[8] Zabielski, L. & Mestel, A. J. 1998. Steady Flow In A Helically Symmetric Pipe. Journal Of Fluid Mechanics, 370, 297-320.

[9] Siggers, J. H. & Waters, S. L. 2008. Unsteady Flows In Pipes With Finite Curvature. Journal Of Fluid Mechanics, 600, 133-165.

[10] Simon, H. A., Chang, M. H. & Chow, J. C. F. 1977. Heat Transfer In Curved Tubes With Pulsatile, Fully Developed, Laminar Flows. Journal Of Heat Transfer, 99, 590-595.

[11] Hydon, P. E. 1994. Resonant And Chaotic Advection In A Curved Pipe. Chaos, Solitons &Amp; Fractals, 4, 941-954.

[12] Timite, B., Castelain, C. & Peerhossaini, H. 2010. Pulsatile Viscous Flow In A Curved Pipe: Effects Of Pulsation On The Development Of Secondary Flow. International Journal Of Heat And Fluid Flow, 31, 879-896.

[13]. Timité, B., Castelain, C. & Peerhossaini, H. 2011. Mass Transfer And Mixing By Pulsatile Three-Dimensional Chaotic Flow In Alternating Curved Pipes. International Journal Of Heat And Mass Transfer, 54, 3933-3950.

[14]. Jarrahi, M., Castelain, C. & Hassan, P. 2011. Laminar Sinusoidal And Pulsatile Flows In A Curved Pipe. Journal Of Applied Fluid Mechanics, Vol. 4. No 2, 21-26.

[15]. Jarrahi, M., Castelain, C. & Peerhossaini, H. 2009. Secondary Flow Velocity Field In Laminar Pulsating Flow Through Curved Pipes-Piv Measurements. Proceedings Of The Asme 2009 Fluids Engineering Division Summer Meeting Fedsm2009, August 2-6, Vail, Colorado Usa.

[16] Timite, B., Jarrahi, M., Castelain, C. & Peerhossaini, H. 2009. Pulsating Flow For Mixing Intensification In A Twisted Curved Pipe. Journal Of Fluids Engineering, 131(12).

NUMERICAL STUDY OF STOKES FLOW OF A NANO FLUID INSIDE A MICRON SIZE NOZZLE

Syed Murtuza Mehdi

ABSTRACT

This paper numerically studies the Stokes flow for a nano fluid with three different nanoparticle void fractions (2.5%, 5% and 7%) inside a straight and smooth micron size nozzle. Flow inside micron size nozzles is characterized by Reynolds number (Re) that remains less than unity (Stokes or creeping flows). In the literature there exist experimental results that validate the macroscopic flow theory inside micron size flow channels, however in most cases the Reynolds number for these experiments were not less than unity which is the essence of Stokes flow. In this study flow inside a micron size nozzle is numerically investigated at ($0.001 \leq Re \leq 0.1$) in order to verify the macroscopic Stokes theory. The effect of Reynolds number, particle size and particle concentration has been studied. It is found that even at these Reynolds number the flow of nanofluid inside a micron size nozzle follows the macroscopic theory of fluid mechanics.

Keywords: *Stokes flow; Micron size nozzle; Mixture model; Laminar flow; Friction factor; Developing length*

1. INTRODUCTION

Stokes flow is characterized by Reynolds number that remains less than unity and is placed under the realm of laminar flows. Laminar flows exist in many important engineering systems of interest. Laminar flows unlike the turbulent flows do not involve any approximations in the mathematics of the motion they deal with, which makes the numerical results for these flows more convincing. Numerous fluid flows and engineering systems involve laminar flows. Either alone or combined with other physical phenomena, laminar flows remains undeniably important. Ultimately laminar flows have been investigated by many researchers for instance Park [1] investigated the effect of square cylinder on laminar wall heat transfer inside a channel, Mehdi and Choi [2] investigated the distribution of Nusselt number at Prandtl number of order 10^{-3} for laminar flow of liquid sodium within the entrance region of a pipe, Farahbaksh et al. [3] numerically investigated the effect of Lorentz force on laminar flow inside a channel, Kim [4] investigated the laminar flow past a rotating sphere in a transverse direction, Tomiyama et al. [5] experimentally investigated the motion of air bubbles in laminar Couette flow, Askari et al. [6] investigated the heat transfer in water at critical pressures under laminar flow regime, Rehman et al. [7] numerically investigated the droplet generation through electrostatic forces under laminar flow regime and Srivastava [8] investigated the laminar flow inside small blood vessels of humans.

According to a review conducted by Tuba and Pidugu [9] micro fluidic devices involves characteristic dimensions that remains within 1 to 1000 μm and usually are governed by Re~O(1) which confirms the existence of laminar flows in these devices. Microfluidics systems are becoming exceedingly important due to the advent of technologies that demands miniaturization, for instance biofluidics, micro mixing devices, inkjet printing and micro-electromechanical systems (MEMS). Single phase experiments conducted by Judy et al. [10] and Jiang et al. [11] have revealed that flow inside micron size circular channels matches well with the macroscopic Stokes theory of fluid dynamics. However, the Reynolds number in their experiments was found to remain higher than unity. On the other hand in certain scenarios for instance, in the case of Srivastava [8] and Jiang et al. [11] the length of the flow channel can become small making the L/D ratio less than 30 (where L is the length of the flow channel and D is its characteristic dimension). Under such circumstances the developing length of the flow can significantly affect the overall performance of the phenomenon taking place inside the device.

Sometimes the fluid flowing inside a micro fluidic device may contain species of other materials for instance nanoparticles. According to Abd et al. [12] liquids containing nano particles are considered to be Newtonian liquids however, according to Rahimi-Esbo et al. [13] the viscosity and density of the nano fluid varies with the concentration of the nanoparticles in the base liquid.

In this study commercial finite element software Comsol Multiphysics has been used to investigate the flow of a nano fluid inside a circular micron size nozzle. The inside diameter of the nozzle was fixed at 410 μm . Two phase mixture model with three different void concentrations (2.5,

Department of Mechatronics Engineering, Jeju National University, Jeju City 690-756, South Korea.
Email: murtuza.mehdi@gmail.com

5 and 7%) was used to simulate the flow. The Reynolds number regime of $0.001 \le \mathrm{Re} \le 0.1$ which essentially satisfies the condition for the Stokes flow was used. In this work we have considered water as a base liquid (solvent) while particle void fractions of 2.5, 5 and 7% are considered for aluminum nano particles having diameter of 25nm. Conventional approach has been used to validate the numerical results with established results of single phase macroscopic fluid dynamics theory. The results show that the flow of a nanofluid (considered in the present study) follows the classical single phase theory of fluid dynamics. On the other hand discrepancies were observed while comparing the developing length of these flows with the available correlation for macroscopic laminar flows.

2. THEORY

The procedure for validating the numerical results with the classical fluid dynamics theory is carried out by calculating the product of the friction factor and the Reynolds number ($f\mathrm{Re}$). This product is then compared with the theoretical value of 64 for single phase fully developed laminar flow. The value of the product fRe is numerically obtained from Eq. (1) as follows.

$$f\,\mathrm{Re} = \frac{2\rho D^3 \Delta p / L}{\mathrm{Re}\mu^2} \tag{1}$$

In Eq. (1) $\Delta p / L$ is the fully developed pressure gradient, ρ is the density and μ is the viscosity of the nanofluid. Flow inside a circular tube becomes fully developed when the pressure gradient reaches a constant value, therefore this approach was utilized in order to numerically estimate the developing length of the flow. The developing length obtained in this way is compared with ($L_t = 0.05 D \mathrm{Re}$). This correlation was found to predict the developing length of laminar flow inside micron size circular tubes by Kandlikar et al [14] in their experimental work. However, in their work the regime of Reynolds number was well above Stokes regime ($500 \le \mathrm{Re} \le 3000$). The equation given in the parenthesis is a famous experimental correlation for single phase macroscopic laminar flows. In this correlation the developing length of the flow is L_t. The viscosity of the nano fluid at different void concentrations is estimated by Eq. (2) as suggested by Krieger and Dougherty [15] and its density is estimated by using Eq. (3) as suggested by Pak and Cho [16].

$$\mu = \mu_{bl}\left(1 - \frac{\alpha}{\alpha_{\max}}\right)^{-2.5\alpha_{\max}} \tag{2}$$

$$\rho = \rho_{bl}(1-\alpha) + \rho_n \alpha \tag{3}$$

In Eq. (2) μ_{bl} is the viscosity of the base liquid (water) and α is the void fraction of the nanoparticles in the solution whereas $\alpha_{\max}$ is the maximum solid void fraction which according to the mixture model in Comsol is limited to 0.62. In Eq. (3) ρ_{bl} is the density of the base liquid (water) and ρ_n is the density of the nano particles (aluminum).

3. NUMERICAL DETAILS

In order to obtain the velocity field inside the computational geometry which is considered to be a smooth nozzle having a length of 12 mm, steady state Navier-Stokes equations based on two phase flow mixture model were numerically solved within Comsol Multiphysics. The mixture model solves for the mixture momentum equations, however it also calculates the velocity field for the discrete solid phase (aluminum nano particles) by assuming a specified velocity slip model (in present case the Hadamard-Rybczynski model which is valid for solid particles if Re ≤ 1). The computational geometry of the problem along with the boundary conditions and part of the axisymmetric grid is shown in Fig. 1 and Fig. 2 respectively.

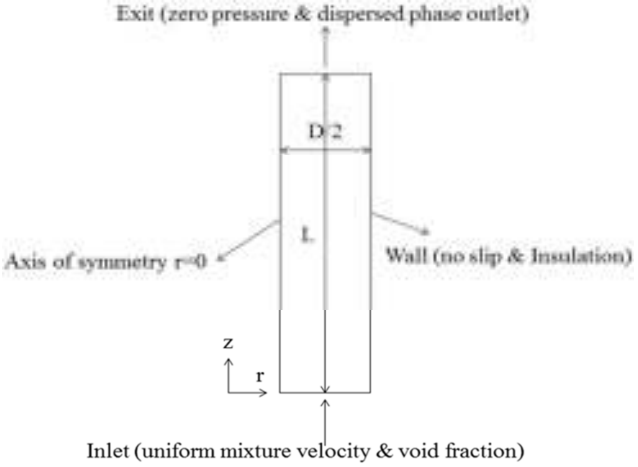

Fig. 1: Computational geometry for the problem.

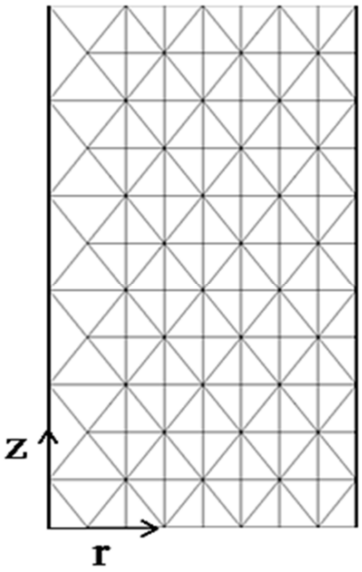

Fig. 2: Part of the axisymmetric computational grid used in this study.

Adaptive mesh refinement was used in this study over a base mesh of 360 unstructured triangular elements. The adaptive mesh refinement technique automatically detects regions with sharp gradients of the solution variables and refines the grid within those regions. Fig. 3 indicates that the relative deviation in the values of fRe continuously drops and eventually becomes negligibly small when the number of mesh refinements reaches seven.

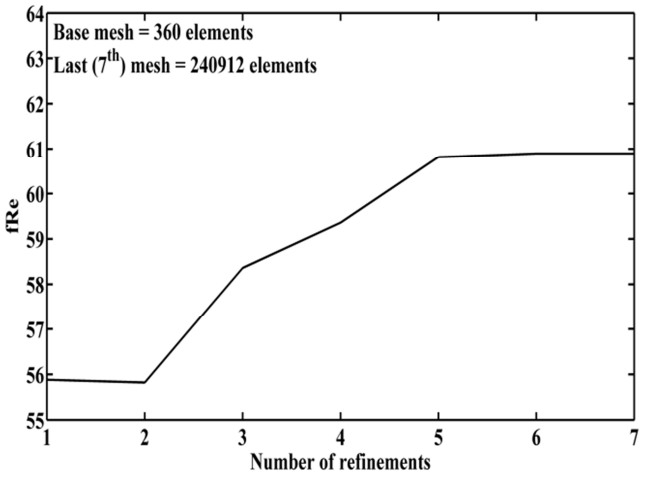

Fig. 3: Relative deviation in fRe with respect to mesh refinements.

Eventually in order to represent the converged results five mesh refinements were chosen for all the cases presented in this study. More details regarding the mixture model can be retrieved from [17].

4. RESULTS AND DISCUSSION

In order to validate the computational model, comparison with the experimental case of Abd et al [12] is shown in Fig. 4.

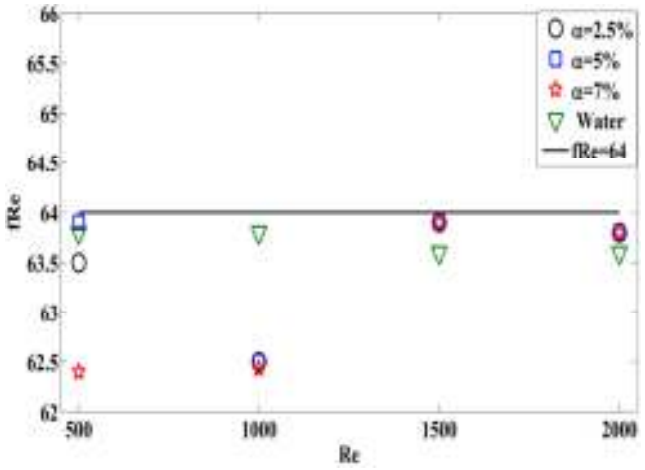

Fig. 4: (Color online) Simulations results for the experimental case of Abd et al [12].

They reported a deviation of 3% from the single phase theory at maximum void fraction of 2.5% which matches well with the simulation results. In Fig. 4 simulation results for higher Reynolds number and void fractions are also shown which were not included in their experiments. These results suggest that the computed value of fRe for the nano fluid matches well with the single phase theory with a maximum of 2.5% error. In addition to this, it can also be noticed from Fig. 5 that the ratio of the pressure gradient at an axial location estimated from the single phase correlation (L_t=0.05DRe) and the simulated fully developed region remains on average at 1.02. This result indicates that the single phase correlation for the developing length remains applicable to the flow of nano fluids under the regime of Re shown in Fig. 4.

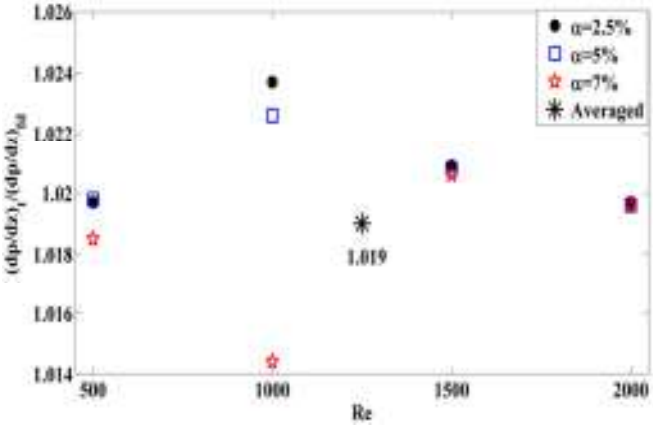

Fig. 5: (Color online) Ratio of pressure gradient at an axial location (z) estimated from the single phase theory (0.05ReD) and fully developed region of the simulations.

In Fig. 6 results for fRe for the same void fractions are presented for the case of micron size nozzle (D=410μm and L=12mm) but for $0.001 \leq Re \leq 0.1$.

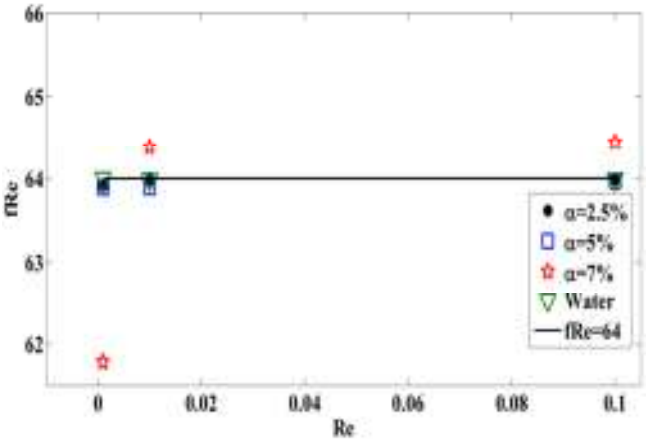

Fig. 6: (Color online) fRe vs Re for different void fractions for micron size nozzle of diameter 410 μm.

It can be seen from Fig. 6 that the simulation results again matches with the macroscopic single phase theory with less than 1% error. Also Fig. 7 indicates that there is no effect of the particle void fraction as well as the Reynolds number on the developing length of the flow.

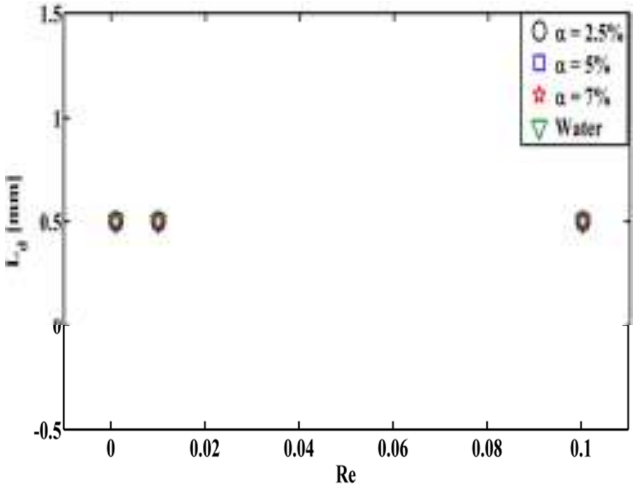

Fig. 7: (Color online) L_d vs Re at different void fractions for micron size nozzle of diameter 410 μm.

The values of fRe are also shown to match with the macroscopic single phase theory when the nano particle size (diameter) was increased up to 100nm from an initial size of 25nm. This effect is shown in Fig. 8.

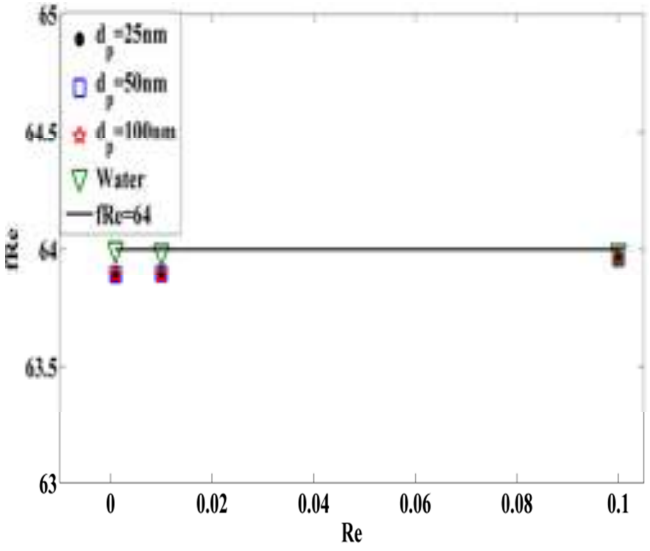

Fig. 8: (Color online) fRe vs Re at different values of nano particle diameter (d_p) for micron size nozzle (D=410μm and α =5%).

However, it is interesting to note that this time the developing length estimated through simulations (as indicated in Fig. 7) does not match with the macroscopic single phase correlation (L_t=0.05DRe). This indicates that within the regime of the Reynolds number considered in this work ($0.001 \le Re \le 0.1$) the developing length becomes independent of the Reynolds number. Although, the effect of the developing length in this study remains negligible, it can become important when the ratio L/D becomes smaller than 30. Considering this fact a correlation is presented in Fig. 9 that relates the developing lengths of the flow of a nano fluid at $0.001 \le Re \le 0.1$ for three different micron size nozzles.

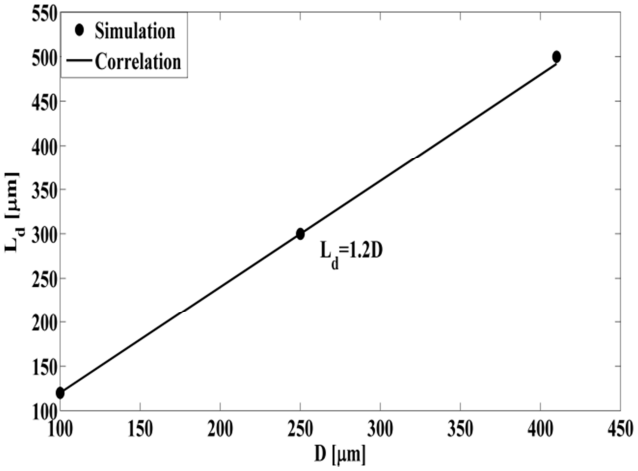

Fig. 9: Correlation between developing length L_d and diameter D of micron size nozzles for $0.001 \le Re \le 0.1$.

It can be seen that the developing length of these flows increases linearly as the diameter of the nozzle is increased.

5. CONCLUSIONS

In this paper Stokes flow for a nano fluid within $0.001 \le Re \le 0.1$ inside a circular micron size nozzle with a diameter of 410μm and length of 12mm has been numerically studied. The base liquid considered is water with three different void fractions of aluminum nano particles (2.5, 5 and 7%). Following conclusions are drawn from the study:

1) The numerical values of fRe matches with the macroscopic theoretical value of 64 with less than 3% error which indicates that even at Reynolds number of order of 10^{-3} the Stokes theory is valid for frictional pressure drop.

2) The nano particle void fraction has no effect on the computed values of fRe. Therefore for the regime of Reynolds number considered in this study the liquid properties of the nano fluid can be replaced simply by the properties of the base liquid making it a single phase fluid flow.

3) For a given liquid, the developing length is found to be independent of both the Re and the particle void fractions and cannot be estimated from the correlation ($L_t = 0.05 Re D$). Therefore, a simple correlation of the form (L_d = 1.2D) has been proposed.

4) For a given liquid, when the order of the Re lies between 10^{-3} and 10^{-1} the developing length increases linearly with the nozzle diameter. Also the nano particle size (diameters) has no effect on the computed values of fRe.

REFERENCES

[1] T. S. Park, Effects of an inserted square cylinder on wall heat transfer in laminar channel flows, Journal of Mechanical Science and Technology, vol. 27, No 5, pp. 1501-1508, 2013.

[2] S. M. Mehdi and K. H. Choi, Heat transfer coefficient for liquid sodium in developing laminar flow regime, Proc. of International Conference on Energy and Sustainability, Karachi, Pakistan pp. 157-160, 2013.

[3] I. Farahbakhsh, A. Paknejad, H. Ghassemi, Numerical simulation of 2-D laminar flow subjected to the Lorentz force effect in a channel with backward-facing step, Journal of Mechanical Science and Technology, vol. 26, No. 10, pp. 1501-1508, 2013.

[4] D. Kim**,** Laminar flow past a sphere rotating in the transverse direction, Journal of Mechanical Science and Technology, vol. 23, No. 10, pp. 578-589, 2009.

[5] A. Tomiyama, H. Tamai, I. Zun and S. Hosokawa, Transverse migration of single bubbles in simple shear flows, Chemical Engineering Science, vol 57 pp. 1849-1858, 2002.

[6] I. B. Askari, S. A. G. Nassab, M. Peymanfard, Numerical investigation of fluid flow and heat transfer for laminar water flow in a duct at critical pressure, Iranian Journal of Science & Technology Transaction B-Engineering, vol. 33, No. 3, pp. 285-290, 2009.

[7] K. Rahman, J. B. Ko, S. Khan, D. S. Kim and K. H. Choi, Simulation of droplet generation through electrostatic forces, Journal of Mechanical Science and Technology, vol. 24, pp. 307-310, 2010.

[8] V. P. Srivastava, A theoretical model of blood flow in small vessels, Application and Applied Mathematics, vol. 2, pp. 51-65, 2007.

[9] B. Tuba and S. B. Pidugu (2006). Characterization of liquid flows in microfluidic systems. International Journal of heat and mass transfer, vol. 49, pp. 815-824, 2006.

[10] J. Judy, D. Maynes and B. W. Webb. Characterization of frictional pressure drop for liquid flows through micro channels, International Journal of heat and mass transfer, vol. 45, pp. 3477-3489, 2002.

[11] X. N. Jiang, Z. Y. Zhou, X. Y. Huang and C. Y. Liu (1997), Laminar flow through microchannels used for microscale cooling systems, IEEE/CPMT Electronic Packaging Technology Conference, pp. 119-122, 1997.

[12] A. Abd, K. S. Al-Jabair and K. Sultan, Experimental investigation of heat transfer and flow of nano fluids in horizontal circular tube. World Academy of Science Engineering and Technology, vol. 61, pp. 484-491, 2012.

[13] M. Rahimi-Esbo, A. A. Ranjbar, A. Ramiar and M. Rahgoshay, Numerical simulation of forced convection of nano fluid in a confined jet, Heat and Mass Transfer, vol. 48, pp. 1995-2005, 2012.

[14] S. G. Kandlikar, S. Joshi, S. Tian, Effect of channel roughness on heat transfer and fluid flow characteristics at low Reynolds numbers in small diameter tubes, Proc. of NHTC01 35th National Heat Transfer Conference, Anaheim, California, 2001.

[15] I. M. Krieger and T. J. Dougherty, A mechanism for non-Newtonian flow in suspensions of rigid spheres. Transactions of the society of Rheology, vol. 3, pp. 137-152, 1959.

[16] B. C. Pak and Y. I. Cho (1998), Hydrodynamic and heat transfer study of dispersed fluids with submicron metallic oxide particles. Experimental Heat Transfer, vol. 11, pp. 151-170, 1998.

[17] Comsol Multiphysics Chemical Engineering Module Users Guide.

COMPUTING ANGULAR CORRELATION FUNCTION USING MESSAGE PASSING INTERFACE

Fareed Ahmed Jokhio[*,**], Umair Ali Khan[*], Intesab Hussain Sadhayo[*]

ABSTRACT

There are many fields of science where the Two- Point Angular Correlation Function (TPACF) is used, such as in statistics, and astronomy. In cosmology, it is used to calculate the distribution of galaxies. The number of galaxies in the Universe is more than 170 billion in a limited region of 13.8 billion light years distance. To compute the distribution of such a large number of galaxies requires huge computational resources. This paper adopts a parallel processing approach to compute angular correlation function. The distribution of galaxies using the TPACF is computed by using a message passing programming model in a cluster based parallel processing environment. To get a better speedup, we adopt a coarse grain approach in which the computation is split among different processes. Each process gets a fixed number of data lines and performs the required computation. The results indicate that the parallel processing of the TPACF provides a significant speedup in terms of execution time.

Keywords: *Parallel processing, TPACF computation, Message Passing Interface, cluster computing, galaxies distribution in the Universe.*

1. INTRODUCTION

The earth is a very small planet and it is a part of a solar system. This solar system is a member of a galaxy having 300 to 400 billion stars [1][2]. At the present time, only a fraction of the Universe is known. According to some estimates the number of galaxies in the known Universe is more than 170 billions [3]. The galaxies have significantly different sizes in terms of the number of stars which count hundreds of billions in each galaxy. To determine at what extent galaxies are distributed, we use the Two-Point Angular Correlation Function (TPACF) [4], which is the relative probability to find the angular distance of galaxies [5] . To understand the structure of the Universe, there exists a theoretical model known as "Labmbda Cold Dark Matter" (∧CDM) [6][7]. According to this model, there are two components in the Universe: (i) dark energy or dark matter which is about 96% of the total matter energy in the Universe and (ii) a normal baryonic matter which is 4%. The dark matter-energy cannot be directly observed. However, we can observe its effects on the other objects in terms of gravitational force. The search for dark matter is a continuous process. However, there is no significant breakthrough. Scientists have already performed several experiments with different kinds of equipments. On the basis of theoretical assumptions, it is believed that the dark matter takes the form of some kind of particles named as "Weakly Interacting Massive Particles" [8], or WIMPs. These particles are present everywhere. But, it is not possible for us to have a trace of them without very sensitive equipments. To hunt the dark matter, scientists use three possible ways. The first way is to explore the space. Scientists use the Alpha Magnetic Spectrometer (AMS) detector which searches for the scattered remains of the dark matter which are formed after the collision of the dark matter particles. In the second method scientists believe that the dark matter can be created by smashing particles together with the Large Hadron Collider. In the third possible method the hunt of dark matter is performed underground by using highly sensitive detectors such as the Large Underground Xenon (LUX).

As a very large number of galaxies in the Universe exists. The distribution of the galaxies in the Universe is determined by the two-point angular correlation function. The knowledge about the distribution of galaxies is particularly important in the sense that it may provide some theoretical basis about the presence of the dark matter. As the number of the galaxies is very large, computing the angular correlation of the galaxies requires substantial computing time. The main focus of this work is to compute the angular correlation of the galaxies using a parallel processing approach.

The remaining parts of this paper are organized as follows: In section II we provide the problem statement. Section III discusses the parallelization of the sequential implementation of the program which computes the distribution of the galaxies. Results are discussed in section IV. Some related works are given in section V, and conclusion is provided in section VI.

* Department of Computer Systems Engineering, Quaid-e-Awam University of Engineering, Science & Technology, Nawabshah, Pakistan

** Department of Information Technologies, Åbo Akademi University, Finland

Email:{fajokhio, umair.khan, intesab}@quest.edu.pk

2. PROBLEM STATEMENT

The main goal of this work is to parallelize the computation of the TPACF, which is used to calculate the distribution of the galaxies in the Universe. The following subsections provide more details about the problem

A. Input data

In order to determine the statistical properties of the distribution of the galaxies, the input datasets are available on the MPA Numerical Cosmology Data Archive. In this work, it is assumed that the earth is the central point of the Universe as shown in Figure 1.

The input data used in this work consists of positions of galaxies between 0.345 and 0.355 redshift. The angular separation between two galaxies is used to determine the distance between them. Input data consists of a list of positions of the galaxies in the equatorial coordinate system (Ra, Dec), where the position is a pair of right ascension and declination. The equatorial coordinates are converted to cartesian coordinate system with x, y and z axis.

B. Computing angles

In this work, the angle between two galaxies is used to determine how much they are separated

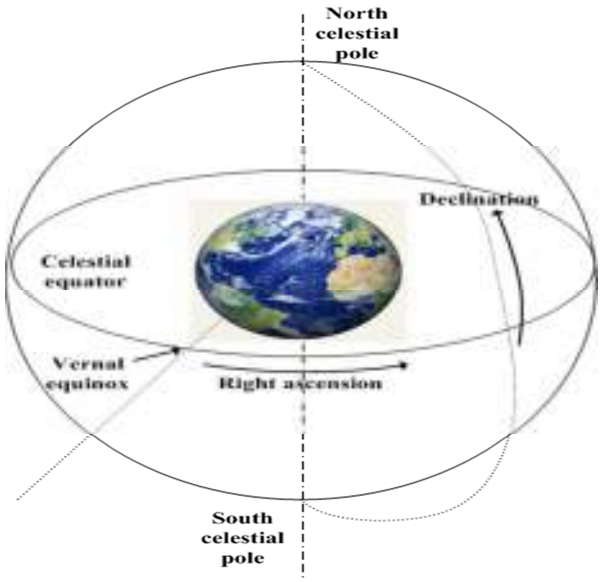

Fig.1. The Universe

from each other. The angle between two galaxies located at point 'p' and 'q' is calculated as,

$$\theta = arcos(p.q) = arcos(x_p x_q + y_p y_q + z_p z_q) \quad (1)$$

Where (x_p, y_p, z_p) are the coordinates of a galaxy located at an observation 'p'. The angle between pairs of galaxies is computed in two sets of observations. A histogram is used to record the distribution of the angles between galaxies. It shows the number of galaxies in a certain range of angular separation.

C. Datasets

In the experiments, two different datasets are used. The first dataset is the real data 'D' which consists of the real observations of galaxies coordinates in the Universe. The other dataset 'R' is a randomly generated set of galaxy coordinates. The idea of using both real and random data is to see if the real galaxies are in an indiscriminate group in space than in a random distribution. If the galaxies are lumped together, then it indicates that there is a gravitational force which is caused by cold dark matter. This gravitational force causes more forces than the actual visible mass of the galaxies. If the galaxies are not lumped together, then it indicates the absence of the dark matter.

D. Constructing histograms

The program calculates the histogram distribution of angular separations between 0 and 64 degrees with a resolution of 0.25 degrees. The number of bins in the histograms is 4*64 = 256. Three histograms are calculated:

(i) HistogramDD(θ) is the number of coordinate pairs (p,q) with an angular separation 'θ', where both observations 'p' and 'q' are from the set of real observations.

(ii) HistogramDR(θ) is the number of pairs (p,q) with an angular separation 'θ', where observations 'p' are from the set of real observations and 'q' are from the randomly generated set.

(iii) HistogramRR(θ) is the number of pairs (p,q) with an angular separation 'θ', where both observations 'p' and 'q' are from the set of randomly generated coordinates.

The histogram computations have a complexity of $O(N^2)$ where 'N' is the number of observations, we compute the angle for all coordinate pairs. It means that the larger datasets require very high computation.

E. Calculating the correlation

The two-point angular correlations 'ω' for angle 'θ' is defined as:

$$\omega(\theta) = 1 + \frac{N^2_{random} \times DD(\theta)}{N^2_{real} \times RR(\theta)} - \frac{2N_{random} \times DR(\theta)}{N_{real} \times RR(\theta)} \quad (2)$$

Where 'N_{real}' and 'N_{random}' are the number of galaxies in the real and random datasets, respectively. DD(θ), DR(θ) and RR(θ) are the histogram values for the angle 'θ'. A positive value of ω(θ) indicates that there are more galaxies with an angular separation 'θ' than expected in a random distribution. A negative value of ω(θ) indicates that there are less galaxies with an angular separation 'θ' than expected in a random distribution. If ω(θ) = 0 the distribution of galaxies is random.

3. PARALLELIZATION

In order to parallelize the sequential implementation of the program, we first profiled the code using gprof [9] so that hotspots or critical regions of the program can be identified. The program was profiled with a small dataset and the profiling results indicate that 87.02% of the execution time is consumed in calculating histogram and remaining 12.98% of the execution time is in the main function. If we analyze the code carefully, we will identify that the critical region, i.e., the histogram calculation is performed for histogramDD, histogramDR, and histogramRR. For histogramDD(real, real) and histogramRR(rand, rand) data points is a triangle of dots. After calculating (i, j) points DD and RR histograms are multiplied by 2, since (j, i) points are not calculated. The histogram calculations for histogramDR(real, rand) is a square (rectangle) of dots.

To get a better speedup, we split the histogram calculations among different processing units. Each processing unit gets a fixed number of data lines from the set of data points and performs the histogram computation. The histogramDR has a square (rectangular) shape. Therefore, it is possible to divide the equivalent amount of work among the processing units. In histogramDD and histogramRR the lines in the lower section have less points. We also divided the equivalent number of lines among processing units regardless of the number of points in the lines. Dynamic load balancing schemes can also be a good solution in a master/slave arrangement by using MPI. The dynamic load balancing schemes are good when the computation requirements are changing. However, in the use case of TPACF, the number of data points is already known, Hence, this paper used the static scheme based on equal number data lines for load balancing.

There are several models of computations available for parallel programming such as shared memory programming model [10], message passing [11], dataflow programming model [12], actor model [13] etc. Detailed description of all those programming models and different programming languages is out of scope here. The sequential source code is modified and re-written using the Message Passing Interface (MPI) [14]. There exist some other programming languages to write parallel programs such as Intel Cilk Plus and OpenMP. However, these programming languages are not suitable to write programs which can execute in a cluster based environment with a distributed memory system. In contrast an MPI based implementation has more portability and can execute on a multicore machine, in a cluster of computing nodes or even in a cloud computing environment.

To execute the parallel version of the code, at least two processes are created and mapped on different processors or processing cores. The one process serves as a master while the second as a slave. The number of slaves can be larger as well. The master performs the task of data distribution to slaves, while slaves perform the actual computation. Each process has a unique "rank" which is an integer starting from 0,1,2 up to N-1.

Figure 2 provides the flow chart of an MPI based program. Here the master process tasks include data partitioning, sending data to the slaves, receiving results from the slaves and finally producing the final output of the program. Each slave obtains data from the master and performs the histogram computation on that part of data and sends the results to the master. Figure 3 shows the part of the code which is used to compute the histogram and is executed at slave side. To compute different histograms such as HistDD, HistDR, and HistRR add_histogram function is invoked with different parameters. Here 'xd_real',' yd_real',' zd_real' indicates the 'x', 'y', 'z' coordinates of a point from the real dataset, while 'xd_sim', 'yd_sim', 'zd_sim' indicates the 'x', 'y', 'z' coordinates of a point from the randomly generated dataset. Both 'i' and 'j' indicates the first and second points respectively. The code for add_histrogram is shown in Figure 4. The histogram computation code is exactly the same for all types of histograms. The only difference is in the arguments sent to perform the computation. Each slave gets a starting data line number and ending data line number to perform the computation.

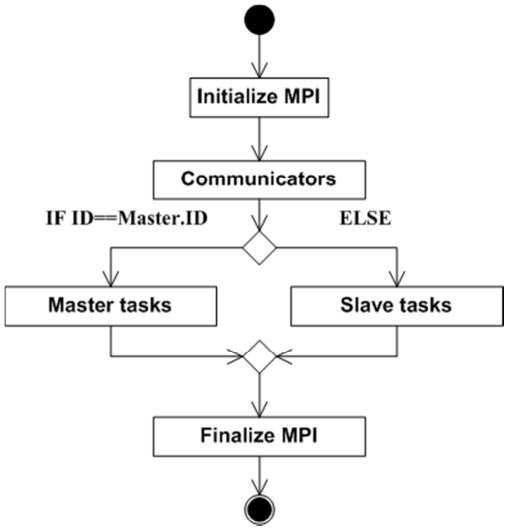

Fig. 2. MPI based program

4. RESULTS AND DISCUSSION

To perform the computation, we use a cluster with 8 compute nodes Each node has 2 Intel Xeon X5650 processors. Each processor has 6 cores with hyperthreading support. Each node has a 24 GB (Gigabytes) of RAM (Random Access Memory). For communication among different nodes, a 4xQDR (Quad Data Rate) infiniband network is used. The cluster also has a 24 TB (Terabytes) disk server.

We test the MPI framework with two datasets, namely small and medium. The small dataset has 20000 coordinates. The medium dataset has 100000 coordinates. The main purpose of this work is to compute the two-point angular correlation function using parallel processing. Our MPI based solution can work on multicore systems, clusters, and in a cloud computing environment without changing the code.

```
/* Initialize the histograms to zero */
 for ( i = 0; i <= nr_of_bins; ++i )
  {
   histogramDD[i] = 0L;
   histogramDR[i] = 0L;
   histogramRR[i] = 0L;
  }

 int x,start,end;
 x = Nooflines_Real/np;
 start = me*x;
 end = x + start;
 if(me==(np-1))
 end = Nooflines_Real;
 for(i=start;i<end;++i)
   {

   for ( j = i+1; j < Nooflines_Real; ++j )
     {

/* Histogram DD compuation */
          dd_histogram (xd_real[i], yd_real[i], zd_real[i], xd_real[j], yd_real[j], zd_real[j], histogramDD, pi, costotaldegrees);


     }
  }
 for(i=start;i<end;++i)
   {
   for ( j = 0; j < Nooflines_Sim; ++j )
     {
      /*Histogram DR compuation */


          add_histogram (xd_real[i], yd_real[i], zd_real[i], xd_sim[j], yd_sim[j], zd_sim[j], histogramDR, pi,
costotaldegrees);
```

```
    }
  }
  for(i=start;i<end;++i)

  {
    for ( j = i+1; j < Nooflines_Sim; ++j )
    {
      /* Histogram RR computation */
          add_histogram (xd_sim[i], yd_sim[i], zd_sim[i], xd_sim[j], yd_sim[j], zd_sim[j], histogramRR, pi, costotaldegrees);

    }
  }
```

Fig. 3. Computation performed by slaves

```
void add_histogram (
float px, float py, float pz, float qx,
float qy, float qz, long int *histogram,
const float pi, const float costotaldegrees)
{
  float theta;
  float degreefactor = 180.0/pi*binsperdegree;
  int bin;
  theta = px*qx + py*qy + pz*qz;
  if ( theta >= costotaldegrees ) {
  /* Skip if theta < costotaldegrees */
    if ( theta > 1.0 ) theta = 1.0;
    /* Calculate which bin to increment */
    bin = (int)(acosf(theta)*degreefactor);
    histogram[bin]++;
  }
}
```

Fig. 4 Histogram Computation

In order to compute the TPACF and determine the distribution of galaxies, two different datasets are used in the experiments. First dataset is the real data 'D' which consists of the real coordinates of the galaxies in the Universe, while the other dataset is a randomly generated set of galaxies coordinates. The real data 'D' basically indicates a subset of the real observations of galaxies coordinates in the known Universe. To determine the presence of dark matter, we plot the histograms for both real and randomly generated data. If the real data has a random distribution of galaxies, it indicates that there is no gravitational force among them and the dark matter does not exist. If the galaxies are in an indiscreimate group in space and they are not randomly distributed, then it indicates the presence of gravitational forces which are caused by cold dark matter. Those gravitational forces make it possible for galaxies to remain closer to each other. To represent the distribution of the galaxies in the Universe, we plot a bar chart graphical representation that organizes the galaxies into logical ranges. This grouping of data points or galaxies coordinates is termed as a histogram. Figures 5 and 6 indicate the histogram results of the two-point angular correlation for a small and medium datasets. HistDD indicates the histogram of the two-point angular correlation of the "real, real" coordinates of the galaxies in the Universe. HistRR indicates the histogram of the two-point correlation of the randomly generated coordinates "rand, rand". HistDR indicates the histogram of the two-point angular correlation for "real, rand" coordinates.

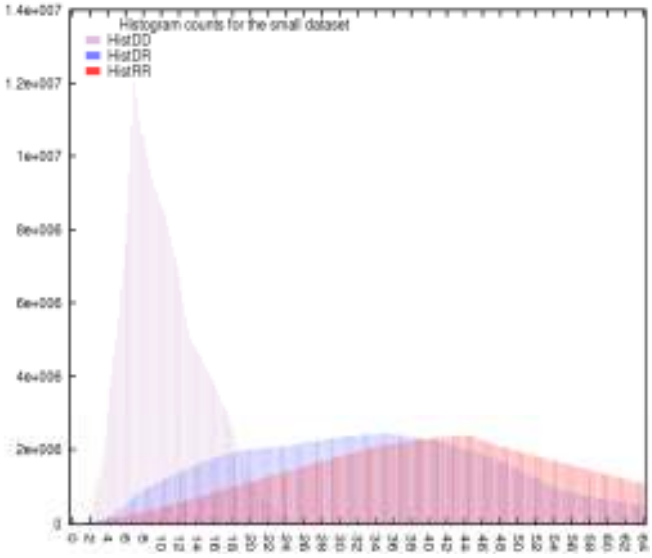

Fig. 5. Histogram for a small dataset

Figure 5 shows that the real galaxies which are indicated in histDD are more lumped together as compared with the random distribution. In the small dataset the distribution of galaxies is mostly between 2 degrees to 25 degrees, though it clearly indicates the presence of dark matter.

To justify the claim, a medium dataset histogram result is indicated in Figure 6. The distribution of galaxies in the medium dataset also depicts the similar pattern as it was in the small dataset. Here, histDD indicates the galaxies are lumped together.

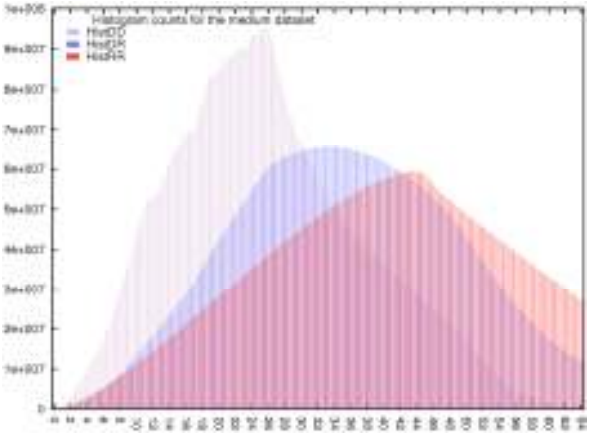

Fig.6. Histogram for a medium dataset

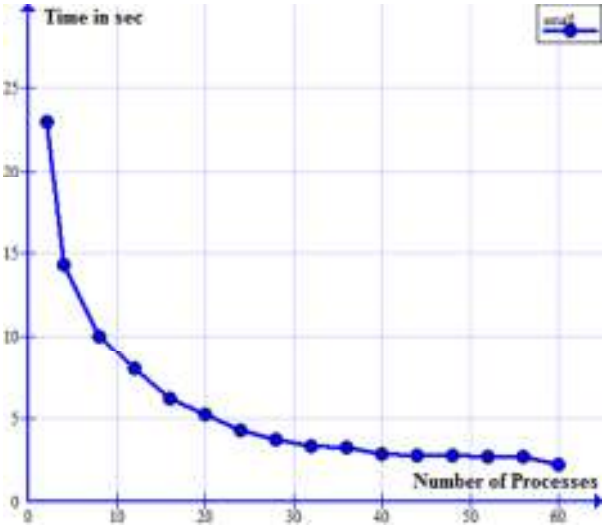

Fig.7. Results for small dataset

Figure 7 shows the execution times for the small dataset with different number of processes. Here we can clearly see that as the number of processes increases, we get better performance. Here the processes are mapped on different cores of the computing nodes on our cluster. In order to evaluate our approach, we also tested the same program on a dataset which requires more computing power as compared with the small dataset.

Figure 8 shows the results for medium dataset and it has more data points as compared with the small dataset. Here we can also see a speedup in execution time. Since the

cluster used for doing experiments has total 08 computing nodes. Each node has 02 processors and each processor has 06 cores. Hence, this system is basically a cluster of multicore machines. In a multicore system, usually there is a shared system bus and shared cache among different cores. Therefore, memory intensive applications do have resource contention and do not scale well [15] . Therefore, the figure 8 which represents the computation time for a medium dataset does not have similar cure as compared with the curve in figure 7.

In our implementation, the first slave process gets the maximum work load and the last slave process gets the shortest work load. It will be more cost efficient to map the master process and the last slave process on the same physical core or processor. In this implementation, the master process mainly partitions the data and send it to the slaves and finally waits to receive the computing results from the slaves. Therefore, mapping the master and the last slave processes on the same physical core will not have any significant effect on the performance.

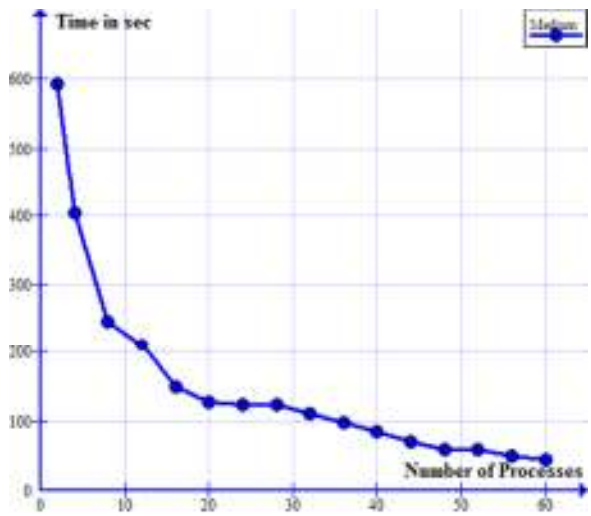

Fig. 8. Results for medium dataset

The results in Figure 7 and 8 indicate that the parallel processing approach to compute the TPACF is also scalable, and can be used for larger datasets and thousands of computing nodes with several processing cores can be used to perform the computation.

5. RELATED WORKS

There exist several works on accelerating TPACF on different platforms such as GPUs, FPGAs and Clusters of computing nodes. In addition to that there also exist some works, which attempt to optimize the algorithm of computing TPACF in less time. Landy et. al. [5] presented a method to quickly calculate the variance and bias for the angular correlation function $\omega(\theta)$, based on the number of pairs of galaxies (DD), random distribution (RR), and on the cross-correlation between the galaxies and random distribution (DR). Although, their method can be used to calculate the bias and variance in shorter time. However, their work is not based on the parallel programming. The work in this paper provides a parallel processing approach to perform the TPCAF computation. Dolence at al.[16] developed an algorithm to perform the computation of two point correlation functions. The parallel algorithm is based on a dual-tree and it requires a very huge amount of memory. To overcome the memory requirements, each data set is broken into smaller sets. This breaking of dataset introduces its own overheads and entire data set is frequently accessed. Kindratenko et al. [17] presented the implementation of TPACF computation on FPGAs. In the experiments 97K dataset was used and two different FPGA designs were evaluated. The obtained speedup was 3.3x and 6.7x as compared with the reference implementation running on an AMD Opteron machine with 2.4 GHz microprocessor. In a similar work using FPGAs Kindratenko et al. [18] claimed a speedup of more than 90x as compared with their sequential implementation running on a single CPU. FPGAs could provide some speedup for 97K dataset. However, if the size of the data set will be in the millions then the current technology of FPGAs will not be able to perform the computation. To compare the performance of a CPU and FPGA, Jatin et al. [19] optimized the TPACF algorithm and executed it on a single node. Their optimized implementation for the 97K particles dataset is 80x faster as compared with the FPGAs performance. There also exist some implementation GPUs [20] which gives better performance as compared with CPU based implementations. Jatin et al. [19] worked on scaling the TPACF computation on a very large number of nodes while using very huge datasets. They claim that the obtained speedup is 35x to 37x as compared with other state-of-the-art parallelization techniques to compute TPACF. It is not possible to cover all related work. However, most works are either platform specific or use optimizations. In contrast, this paper proposes a generic parallel processing approach to computing TPACF in a parallel computing environment.

6. CONCLUSION

This paper presented a parallel implementation of the two-point angular correlation function by using an MPI programming model. The approach is evaluated using a master/slave communication model. The most compute intensive operation of the correlation functions is the computation of different histograms. To distribute the data for the histogram computation among different slaves, an equivalent number of data lines are taken into account. The results indicate that the parallelization approach gets a higher speedup in terms of execution time as the number of processes are increased. A potential future work of this

work is a comparison between shared memory models and distributed memory models for multi-core systems for this application.

REFERENCES

[1] R. E. Nancy and W. Mark, "The Mass of the Andromeda Galaxy," Royal Astronomical Society, vol. 316, no. 1, pp. 1-16, 13 April 2000.

[2] X. X. Xiang, W. R. Hans, b. Z. Gong, R. F. Paola, N. Thorsten, S. Matthias, V. d. B. Frank C, C. B. Timothy, W. L. Young, F. B. Eric, M. R. Constance, Y. Brian, J. N. Heidi, W. Ronald, K. Xi, W. L. S. Matthew and P. S. Donald, "The Milky Way's Circular Velocity Curve to 60 kpc and an Estimate of the Dark Matter Halo Mass from Kinematics of ~2400 SDSS Blue Horizontal Branch Stars," The Astrophysical Journal, vol. 684, no. 2, pp. 1-42, 28 May 2008.

[3] D. Deutsch, The Fabric of Reality, UK: Penguin Books Limited, 14 April 2011.

[4] X. Chen and J. Hakkila, "The Two-Point Angular Correlation Function and BATSE Sky Exposure," Dec 1997.

[5] S. D. Landy and A. S. Szalay, "Bias and Variance of Angular Correlation Functions," Astrophysical Journal, vol. 412, pp. 64-71, 1993.

[6] B. Luc and L. T. Alexandre, "Model of dark matter and dark energy based on gravitational polarization," p. 4, 02 July 2008.

[7] D. Aharon, K. David and L. Yoav, "Cold dark matter from dark energy," p. 4, 29 November 2001.

[8] G. S. Alex and M. K. Sawas, "Exclusion of canonical WIMPs by the joint analysis of Milky Way dwarfs with Fermi," p. 5, August 2011.

[9] S. L. Graham, P. B. Kessler and M. K. McKusick, "gprof: a call graph execution profiler," ACM SIGPLAN Notices, vol. 39, no. 4, pp. 49--57, April 2004.

[10] A. R. Kay and R. Steven, UNIX Systems Programming: Communication, Concurrency, and Threads, Prentice Hall Professional, 2003.

[11] M. M. John and C. W. David, "Some considerations for a high performance message-based interprocess communication system," in Proceedings of the 1975 ACM SIGCOMM/SIGOPS workshop on Interprocess communications, New York, NY, USA , 1975.

[12] M. J. Wesley, R. P. H. J and J. M. Richard, "Advances in Dataflow Programming Languages," ACM Computing Surveys, vol. 36, no. 1, pp. 1-34, 2004.

[13] G. A. Agha, "ACTORS: A Model of Concurrent Computation in Distributed Systems," MIT Libraries, Cambridge, United States, 1985.

[14] "MPI: A Message-Passing Interface," University of Tennessee, Knoxville, Tennessee, May 5, 1994.

[15] H. Robert, J. Haoqiang, M. Piyush, C. Johnny, D. Jahed, G. Sharad, J. Dennis, T. Kenichi and B. Rupak, "Performance impact of resource contention in multicore systems," in Parallel & Distributed Processing (IPDPS), 2010 IEEE International Symposium, Atlanta, Georgia, April 2010.

[16] D. Joshua and J. B. Robert, "Fast Two-Point Correlations of Extremely Large Data Sets," in The 9th LCI International Conference on High-Performance Clustered Computing, Pittsburgh, Pennsylvania, USA, 2008.

[17] V. K. Volodymyr and J. B. Robert, "Accelerating Cosmological Data Analysis with FPGAs," in 17th IEEE Symposium on Field Programmable Custom Computing Machines, Napa, California, 2009.

[18] V. K. Volodymyr, D. M. Adam and J. B. Robert, "Implementation of the two-point angular correlation function on a high-performance reconfigurable computer.," Scientific Programming, vol. 17, no. 3, pp. 247-259, 2009.

[19] C. Jatin, K. Changkyu, S. Hemant and P. Jongsoo, "Billion-Particle SIMD-Friendly Two-Point Correlation on Large-Scale HPC Cluster Systems," in SC '12 Proceedings of the International Conference on High Performance Computing, Networking, Storage and Analysis, Utah, USA, 2012.

[20] W. R. Dylan, V. K. Volodymyr and J. B. Robert, "Accelerating cosmological data analysis with graphics processors," in Proceedings of 2nd Workshop on General Purpose Processing on Graphics Processing Units , Washington, DC, USA, 2009.